Vertex Approximate Gradient Discretization preserving positivity for two-phase Darcy flows in heterogeneous porous media

Konstantin Brenner, Roland Masson, El Houssaine Quenjel

Vertex Approximate Gradient Discretization preserving positivity for two-phase Darcy flows in heterogeneous porous media

February 18, 2020

K. Brenner,[1] R. Masson[1] and E.H. Quenjel[1]

Abstract

In this article, a new nodal discretization is proposed for two-phase Darcy flows in heterogeneous porous media. The scheme combines the Vertex Approximate Gradient (VAG) scheme for the approximation of the gradient fluxes with an Hybrid Upwind (HU) approximation of the mobility terms in the saturation equation. The discretization in space incorporates naturally nodal interface degrees of freedom (d.o.f.) allowing to capture the transmission conditions at the interface between different rock types for general capillary pressure curves. It is shown to guarantee the physical bounds for the saturation unknowns as well as a nonnegative lower bound on the capillary energy flux term. Numerical experiments on several test cases exhibit that the scheme is more robust compared with previous approaches allowing the simulation of 3D large Discrete Fracture Matrix (DFM) models.

1 Introduction

Two-phase Darcy flows are widely used in many subsurface applications such as oil and gas recovery, basin modeling, geological storage, geothermal energy or hydrogeology. These models lead to Partial Differential Equations (PDEs) accounting for strongly coupled nonlinear processes typically involving viscous, buoyancy and capillary forces [6, 18, 39]. The high heterogeneity of natural porous media entails a large range of velocities and time scales in the transport of the phase saturations. Capillary driven flow dynamics can also occur at interfaces between different rock types where highly nonlinear transmission conditions take place. The abrupt change of the pore sizes at such interfaces induces spatially discontinuous capillary pressure curves at the Darcy scale triggering the discontinuity of the phase saturation and pressure solutions [44, 21, 16, 17, 11]. These discontinuities play a major role and should be accurately captured in many important processes such as capillary driven imbibition in oil recovery or capillary barrier effects in oil migration and gas storage. This is particularly enhanced in the case of Discrete Fracture Matrix (DFM) models which exhibit highly contrasted permeabilities and capillary pressure curves between the fracture network and the surrounding matrix domains [9, 35, 42, 38, 34, 12, 13, 2, 31, 14, 1, 3, 45, 4].

The objective of this work is to propose a numerical method for two-phase Darcy flows with the ability to simulate accurately and efficiently large and highly heterogeneous models. Having typically in mind large DFM simulations for which tetrahedral meshes are commonly used to cope with the geometrical complexity of the fracture networks, the discretization in space will be based on nodal degrees of freedoms (d.o.f.). It will provide a much lower number of d.o.f. on tetrahedral meshes than the number of cells for cell-centered discretizations like Multi-Point Flux Approximations (MPFA) [31, 3, 45] or the number of faces for face based

[1]Université Côte d'Azur, Inria, CNRS, Laboratoire J.A. Dieudonné, Team Coffee, Parc Valrose, 06108 Nice cedex 02, France, konstantin.brenner@univ-cotedazur.fr, roland.masson@univ-cotedazur.fr, el-houssaine.quenj@univ-cotedazur.fr

discretizations like the Mixed Hybrid Finite Element (MHFE) method [34, 2] or the Hybrid Finite Volume scheme [1]. The additional asset of nodal discretizations compared with cell centered discretizations is to include d.o.f. at rock type interfaces as long as the mesh is conforming with the heterogeneities of the porous medium. These nodal pressures and saturations unknowns will be used to enforce the Darcy normal flux continuity equations combined with the saturation jump condition [16, 11, 27]. In this work, we will consider the Vertex Approximate Gradient (VAG) discretization developed in [27, 12, 13] for two-phase Darcy flows in heterogeneous media. The VAG scheme is based on nodal d.o.f. like Control Volume Finite Element (CVFE) methods but it also includes the cell d.o.f. which are eliminated at the linear algebra level at each Newton iteration without any fill-in. These cell d.o.f. provide an additional flexibility in the choice of the control volumes in order to avoid mixing different rock types at nodal control volumes. It has been shown in [27] to be more accurate than usual CVFE discretizations.

The time integration will be chosen implicit to avoid severe time step restrictions in high velocity regions such as fractures. It will be also fully coupled to account for the strong coupling between the pressure and saturation unknowns in the transmission conditions at different rock type interfaces. As noticed in [5], the pressure and saturation unknowns cannot be decoupled at such different rock type interfaces to preserve the stability of the discretization.

The selected numerical method should also provide a robust nonlinear convergence of the Newton type solver to allow for large time steps, typically at the time scale of the matrix in DFM simulations. Let us refer to [41, 37] for alternative linearization schemes to the Newton method which aim to the improvement of the nonlinear solver. In this work, the additional nonlinear solver robustness will be first achieved by extension of the Hybrid Upwind (HU) transport scheme to the VAG discretization framework. The HU transport scheme has been introduced in [24, 28] as an alternative to the Phase Potential Upwind (PPU) scheme [10, 22] for the approximation of the mobility terms in the saturation equation. In the framework of Two-Point Flux Approximation (TPFA), it has been recently shown in [32, 33, 4] to provide additional nonlinear convergence robustness thanks to better smoothness properties of the HU two-point monotone fluxes compared with the PPU fluxes. Note that in [33, 4], the transmission conditions at different rock type interfaces are accounted for using a single interface unknown, typically the saturation or capillary pressure. This cannot account for general capillary pressure curves for which the pressure and saturation primary unknowns must remain fully coupled at the interface for the well posedness and stability of the discretization. This motivates the fully coupled approach adopted in this work. The extension of the HU scheme to the VAG discretization has to cope with the non-monotonicity of the Multi-Point VAG gradient capillary flux. It results that the HU numerical flux used for the saturation equation cannot be monotone like in [33, 4] where it is combined with a TPFA of the gradient capillary flux. Nevertheless, it can still be positivity preserving in the spirit of [30, 40] which suffices to guarantee the physical bounds on the saturations as well as the positivity of the capillary energy flux term.

A second ingredient for the robustness of the nonlinear convergence is related to the choice of the primary unknowns at interface nodes between different rock types. Following [13], our choice is based on a generalization of switch of variable techniques allowing to take into consideration general capillary pressure curves including non strictly increasing, typically constant, capillary pressures.

The remaining part of the paper is outlined as follows. In Section 2, the two-phase Darcy flow model is described as well as our assumptions on the data set. Note that the flow will be considered incompressible and immiscible to simplify the presentation and in order to focus on the issues related to the geological complexity of the porous medium. In Section 3, we survey the VAG discretization and the choice of the primary unknowns accounting for general capillary pressure curves at different rock type interfaces. The transport scheme is introduced in a general framework using numerical fluxes with monotonicity and consistency conditions which are shown to guarantee the physical bounds on the saturation unknown and the existence of a solution at fixed total velocity. Two examples of such numerical fluxes are proposed, namely the PPU VAG scheme and the HU VAG scheme. Finally, Section 4 exhibits the additional robustness of the HU VAG scheme compared

with the PPU VAG scheme on several test cases including large and highly heterogeneous DFM models.

2 Two-phase Darcy flow model

Let Ω be a polyhedral bounded domain of $\mathbb{R}^d$ ($d \geq 1$) and $(0, t_f)$ be the time interval. The wetting phase is indexed by w and the non-wetting phase by nw. The porous medium domain Ω is constituted by several rock types partitioning the domain in a set of polyhedral open subsets $(\Omega_{\rm rt})_{{\rm rt}\in\mathcal{RT}}$ such that $\overline{\Omega} = \bigcup_{{\rm rt}\in\mathcal{RT}} \overline{\Omega}_{\rm rt}$, where $\mathcal{RT}$ is the set of rock types. We consider the incompressible and immiscible two-phase Darcy flow model in heterogeneous porous medium defined by the following system of equations set on $Q_{t_f} = \Omega \times (0, t_f)$

$$\left\{\begin{array}{l} \phi(\mathbf{x})\partial_t s^\alpha + {\rm div}\mathbf{V}^\alpha = 0, \\ \mathbf{V}^\alpha = -\eta^\alpha(\mathbf{x}, s^\alpha)\Lambda(\mathbf{x})(\nabla p^\alpha - \rho_\alpha \mathbf{g}), \\ p_c = p^{\rm nw} - p^{\rm w} \in \widetilde{P}_c(\mathbf{x}, s^{\rm nw}), \\ s^{\rm nw} + s^{\rm w} = 1, \end{array}\right. \tag{2.1}$$

with $\alpha \in \{{\rm nw}, {\rm w}\}$. In (2.1) $\phi(\mathbf{x})$ denotes the medium porosity, $\Lambda(\mathbf{x})$ the medium permeability tensor, s^α the phase saturation, p^α the phase pressure, $\mathbf{V}^\alpha$ the phase Darcy velocity, and p_c the capillary pressure. The mass density ρ_α of each phase $\alpha \in \{{\rm nw}, {\rm w}\}$ is assumed constant. The gravity acceleration vector is denoted by $\mathbf{g}$ and its norm by g. The phase mobility function, defined as the ratio of the relative permeability $k_r^\alpha(\mathbf{x}, s^\alpha)$ to the constant phase dynamic viscosity μ^α, is denoted by $\eta^\alpha(\mathbf{x}, s^\alpha)$. We denote by $\widetilde{P}_c(\mathbf{x}, s)$ the monotone graph extension of the capillary pressure function. As prescribed in the following set of assumptions, the dependence on $\mathbf{x}$ of $\widetilde{P}_c$ and of η^α is assumed piecewise constant on each rock type subdomain.

To fix ideas, the system (2.1) is completed by an initial datum on the non-wetting phase saturation and by the boundary conditions

$$\mathbf{V}^\alpha \cdot \mathbf{n} = 0 \quad \text{on } \Gamma^N \times (0, t_f), \quad p^\alpha = p^\alpha_{\rm Dir} \quad \text{on } \Gamma^{\rm Dir} \times (0, t_f) \quad \text{for } \alpha \in \{{\rm nw}, {\rm w}\},$$

where $\mathbf{n}$ is the unit normal vector to Γ^N oriented outward to Ω, and $\{\Gamma^N, \Gamma^{\rm Dir}\}$ a partition of $\partial\Omega$ such that $\left|\Gamma^{\rm Dir}\right| > 0$.

The following assumptions are made on the model's data set. Note that the following restrictions on the capillary pressure curves are motivated to provide a common setting for the proofs of Propositions 3.1, 3.2 and 3.3. In practice, as exhibited in the Numerical Section, the discretizations presented in Section 3 work for general capillary pressure curves including unbounded functions.

($\mathbf{A}_1$) The porosity ϕ belongs to $L^\infty(\Omega)$ with $0 < \underline{\phi} \leq \phi(\mathbf{x}) \leq \overline{\phi}$ for a.e. $\mathbf{x} \in \Omega$.

($\mathbf{A}_2$) The permeability tensor $\Lambda \in L^\infty(\Omega)^{d\times d}$ is symmetric and uniformly elliptic i.e. there exist $\underline{\Lambda}, \overline{\Lambda} > 0$ such that

$$\underline{\Lambda}\,|\mathbf{v}|^2 \leq \Lambda(\mathbf{x})\mathbf{v}\cdot\mathbf{v} \leq \overline{\Lambda}\,|\mathbf{v}|^2 \text{ for a.e. } \mathbf{x} \in \Omega, \text{ for all } \mathbf{v} \in \mathbb{R}^d.$$

($\mathbf{A}_3$) Let $P_{c,{\rm rt}}(s^{\rm nw})$ be a given capillary function for the rock type ${\rm rt} \in \mathcal{RT}$, which is assumed to be continuous, piecewise $\mathcal{C}^1$ and non-decreasing on $[0, 1]$. We define its monotone graph extension by

$$\widetilde{P}_{c,{\rm rt}}(s) = \left\{\begin{array}{cll} \left[-\infty, P_{c,{\rm rt}}(0)\right] & \text{if} & s = 0, \\ P_{c,{\rm rt}}(s) & \text{if} & s \in (0, 1), \\ \left[P_{c,{\rm rt}}(1), +\infty\right] & \text{if} & s = 1, \end{array}\right.$$

and we set

$$\widetilde{P}_c(\mathbf{x}, s) = \sum_{\mathrm{rt}\in\mathcal{RT}} \widetilde{P}_{c,\mathrm{rt}}(s)\mathbb{1}_{\Omega_{\mathrm{rt}}}(\mathbf{x}), \qquad \text{for a.e. } \mathbf{x}\in\Omega,$$

where $\mathbb{1}_{\Omega_{\mathrm{rt}}}$ is the characteristic function of the subdomain Ω_{rt}.

($\mathbf{A}_4$) For each $\alpha \in \{\mathrm{nw}, \mathrm{w}\}$, the mobility function η^α is given by

$$\eta^\alpha(\mathbf{x}, s) = \sum_{\mathrm{rt}\in\mathcal{RT}} \eta^\alpha_{\mathrm{rt}}(s)\mathbb{1}_{\Omega_{\mathrm{rt}}}(\mathbf{x}), \qquad \text{for a.e. } \mathbf{x}\in\Omega,$$

where $\eta^\alpha_{\mathrm{rt}}$ is a non-decreasing continuous function on $\mathbb{R}$ such that $\eta^\alpha_{\mathrm{rt}}(s) = 0$ for all $s \le 0$ and $\eta^\alpha(s) = \eta^\alpha(1)$ for all $s \ge 1$. This extension of the mobilities on $\mathbb{R}$ is required for the proof of the physical bounds on the saturation. It is also used to derive the consistency properties (ii) and (iii) of the numerical fluxes as specified in Remark 3.1.

We assume in addition that the total mobility function $\eta(\mathbf{x}, s) = \eta^{\mathrm{nw}}(\mathbf{x}, s) + \eta^{\mathrm{w}}(\mathbf{x}, 1-s)$ is such that there exists $\eta_{\min} > 0$ with

$$\eta(\mathbf{x}, s) \ge \eta_{\min} \text{ for a.e. } \mathbf{x}\in\Omega \text{ and for all } s\in\mathbb{R}.$$

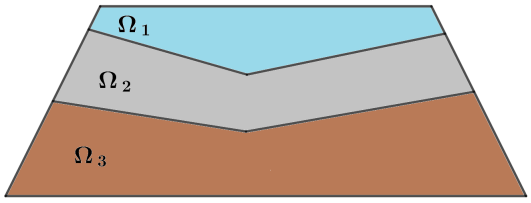

Figure 1: Example of a 2D heterogeneous medium Ω partitioned in three rock type subdomains.

The discretization developed in the next section is essentially based on the total velocity formulation for which we recall the following definition of the total velocity:

$$\mathbf{V}^T = -\sum_{\alpha\in\{\mathrm{nw},\mathrm{w}\}} \eta^\alpha(\mathbf{x}, s^\alpha)\Lambda(\mathbf{x})(\nabla p^\alpha - \rho_\alpha \mathbf{g}). \tag{2.2}$$

This allows to express the phase Darcy velocities at given total velocity $\mathbf{V}^T$ as follows:

$$\begin{aligned}
\mathbf{V}^{\mathrm{nw}} &= f^{\mathrm{nw}}(\mathbf{x}, s^{\mathrm{nw}})\mathbf{V}^T + \frac{\eta^{\mathrm{nw}}(\mathbf{x}, s^{\mathrm{nw}})\eta^{\mathrm{w}}(\mathbf{x}, 1-s^{\mathrm{nw}})}{\eta(\mathbf{x}, s^{\mathrm{nw}})}\Lambda(\mathbf{x})\Big(-\nabla p_c + (\rho_{\mathrm{nw}} - \rho_{\mathrm{w}})\mathbf{g}\Big) \\
&= \underbrace{f^{\mathrm{nw}}(\mathbf{x}, s^{\mathrm{nw}})\mathbf{V}^T}_{\text{fractional flow term}} + \underbrace{\frac{\eta^{\mathrm{nw}}(\mathbf{x}, s^{\mathrm{nw}})\eta^{\mathrm{w}}(\mathbf{x}, 1-s^{\mathrm{nw}})}{\eta(\mathbf{x}, s^{\mathrm{nw}})}(-\Lambda(\mathbf{x})\nabla p_c)}_{\text{capillary term}} \\
&\quad + \underbrace{\frac{\eta^{\mathrm{nw}}(\mathbf{x}, s^{\mathrm{nw}})\eta^{\mathrm{w}}(\mathbf{x}, 1-s^{\mathrm{nw}})}{\eta(\mathbf{x}, s^{\mathrm{nw}})}(\rho_{\mathrm{nw}} - \rho_{\mathrm{w}})\Lambda(\mathbf{x})\mathbf{g}}_{\text{gravity term}},
\end{aligned} \tag{2.3}$$

and $\mathbf{V}^{\mathrm{w}} = \mathbf{V}^T - \mathbf{V}^{\mathrm{nw}}$ with the non-wetting phase fractional flow function defined by

$$f^{\mathrm{nw}}(\mathbf{x}, s) = \frac{\eta^{\mathrm{nw}}(\mathbf{x}, s)}{\eta(\mathbf{x}, s)}. \tag{2.4}$$

As a result of Assumption $(\mathbf{A}_4)$, for $\beta \in \{f^{\rm nw}, \eta\}$, we can readily define the rock type fractional flow $f^{\rm nw}_{\rm rt}$ and total mobility $\eta_{\rm rt}$ functions such that

$$\beta(\mathbf{x}, s) = \sum_{\mathrm{rt}\in\mathcal{RT}} \beta_{\rm rt}(s)\mathbb{1}_{\Omega_{\rm rt}}(\mathbf{x}).$$

3 Positive VAG discretization of two-phase Darcy flows in heterogeneous medium

3.1 VAG fluxes and porous volumes

The VAG discretization of two-phase Darcy flows introduced in [26] considers generalized polyhedral meshes of Ω in the spirit of [25]. It is recalled in the following to fix the notations and for the convenience of the reader.

Let $\mathcal{M}$ be the set of cells that are disjoint open polyhedral subsets of Ω such that $\bigcup_{K\in\mathcal{M}} \overline{k} = \overline{\Omega}$. For all $k \in \mathcal{M}$, $\mathbf{x}_k$ denotes the so-called center of the cell k under the assumption that k is star-shaped with respect to $\mathbf{x}_k$. We then denote by $\mathcal{F}_k$ the set of faces of the cell $k \in \mathcal{M}$ and by $\mathcal{F} = \bigcup_{k\in\mathcal{M}} \mathcal{F}_k$ the set of faces of the mesh. Remark that the faces are not assumed to be planar, hence the term "generalized polyhedral mesh". For $\sigma \in \mathcal{F}$, let $\mathcal{E}_\sigma$ be the set of edges of the face σ and $\mathcal{V}_\sigma$ the set of vertices of σ. We denote by $\mathcal{E} = \bigcup_{\sigma\in\mathcal{F}} \mathcal{E}_\sigma$ the set of all edges of the mesh. For each $k \in \mathcal{M}$ we define the set of nodes of the cell k by $\mathcal{V}_k = \bigcup_{\sigma\in\mathcal{F}_k} \mathcal{V}_\sigma$, and we also denote by $\mathcal{V} = \bigcup_{K\in\mathcal{M}} \mathcal{V}_k$ the set of all vertices of the mesh, and by $\mathcal{M}_\mathbf{s}$, the subset of cells sharing the node $\mathbf{s} \in \mathcal{V}$. It is then assumed that for each face $\sigma \in \mathcal{F}$, there exists a so-called center of the face $\mathbf{x}_\sigma \in \sigma \setminus \bigcup_{e\in\mathcal{E}_\sigma} e$ such that

$$\mathbf{x}_\sigma = \sum_{\mathbf{s}\in\mathcal{V}_\sigma} \beta_{\sigma,\mathbf{s}}\, \mathbf{x}_\mathbf{s}, \text{ with } \sum_{\mathbf{s}\in\mathcal{V}_\sigma} \beta_{\sigma,\mathbf{s}} = 1, \text{ and } \beta_{\sigma,\mathbf{s}} \geq 0 \text{ for all } \mathbf{s} \in \mathcal{V}_\sigma.$$

Moreover the face σ is assumed to be defined by the union of the triangles $T_{\sigma,e}$ defined by the face center $\mathbf{x}_\sigma$ and each edge $e \in \mathcal{E}_\sigma$.

Note also that the mesh is supposed to be conforming w.r.t. the partition of Ω in subdomains $\Omega_{\rm rt}, \mathrm{rt} \in \mathcal{RT}$, and w.r.t. the partition $\{\Gamma^N, \Gamma^{\rm Dir}\}$ of $\partial\Omega$. We then denote by $\mathcal{V}_{\rm Dir}$ the set of nodes located at the boundary $\overline{\Gamma}^{\rm Dir}$.

The VAG discretization has been introduced in [25] for diffusive problems on heterogeneous anisotropic media. It is based on the following vector space of degrees of freedom:

$$X_\mathcal{D} = \{v_k \in \mathbb{R}, v_\mathbf{s} \in \mathbb{R}, k \in \mathcal{M}, \mathbf{s} \in \mathcal{V}\}.$$

A finite element discretization is built using a tetrahedral sub-mesh of $\mathcal{M}$ and a second order interpolation at the face centers $\mathbf{x}_\sigma$, $\sigma \in \mathcal{F}$ defined for all $v_\mathcal{D} \in X_\mathcal{D}$ by

$$I_\sigma(v_\mathcal{D}) = \sum_{\mathbf{s}\in\mathcal{V}_\sigma} \beta_{\sigma,\mathbf{s}} v_\mathbf{s}.$$

The tetrahedral sub-mesh is defined by $\mathcal{T} = \{T_{k,\sigma,e}, e \in \mathcal{E}_\sigma, \sigma \in \mathcal{F}_k, k \in \mathcal{M}\}$ where $T_{k,\sigma,e}$ is the tetrahedron joining the cell center $\mathbf{x}_k$ to the triangle $T_{\sigma,e}$ (see Figure 2).

For a given $v_\mathcal{D} \in X_\mathcal{D}$, we define the function $\pi_\mathcal{T} v_\mathcal{D} \in H^1(\Omega)$ as the continuous piecewise affine function on each tetrahedron of $\mathcal{T}$ such that $\pi_\mathcal{T} v_\mathcal{D}(\mathbf{x}_k) = v_k$, $\pi_\mathcal{T} v_\mathcal{D}(\mathbf{s}) = v_\mathbf{s}$, and $\pi_\mathcal{T} v_\mathcal{D}(\mathbf{x}_\sigma) = I_\sigma(v_\mathcal{D})$ for all $K \in \mathcal{M}$, $\mathbf{s} \in \mathcal{V}$, $\sigma \in \mathcal{F}$. The nodal finite element basis functions associated to this interpolation operator are denoted by $\varphi_k, \varphi_\mathbf{s}$, $k \in \mathcal{M}, \mathbf{s} \in \mathcal{V}$.

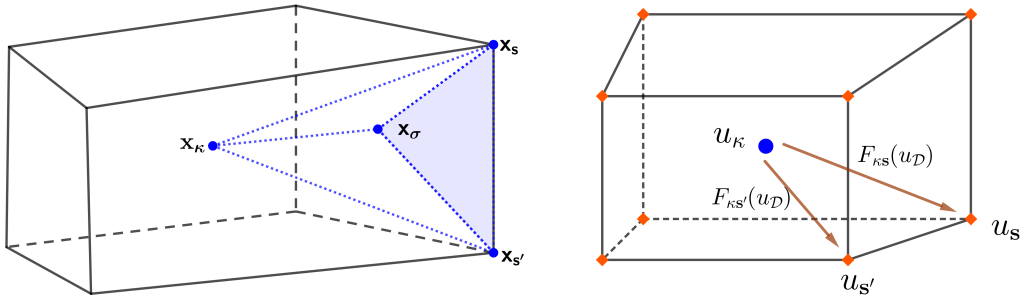

Figure 2: (Left): example of one cell k with a tetrahedron $T_{k,\sigma,e}$ of the sub-mesh $\mathcal{T}$. (Right): example of VAG fluxes in a cell k.

The VAG scheme is a control volume scheme in the sense that it amounts, for each d.o.f. not located at the Dirichlet boundary and each phase, to a volume balance equation. The two main ingredients are therefore the conservative fluxes and the porous volumes. For $u_\mathcal{D} \in X_\mathcal{D}$, the VAG fluxes $F_{k,\mathbf{s}}(u_\mathcal{D})$ connect the cell $k \in \mathcal{M}$ to the nodes $\mathbf{s} \in \mathcal{V}_k$ (see Figure 2). They are derived from the finite element variational formulation (see [25] for details) leading to the following generalized fluxes definition

$$F_{k,\mathbf{s}}(u_\mathcal{D}) = \int_k -\Lambda(\mathbf{x})\nabla\pi_\mathcal{T} u_\mathcal{D} \cdot \nabla\varphi_\mathbf{s} d\mathbf{x} = \sum_{\mathbf{s}'\in\mathcal{V}_k} \mathbb{T}_k^{\mathbf{s},\mathbf{s}'}(u_k - u_{\mathbf{s}'}), \tag{3.1}$$

with

$$\mathbb{T}_k^{\mathbf{s},\mathbf{s}'} = \int_k \Lambda(\mathbf{x})\nabla\varphi_{\mathbf{s}'} \cdot \nabla\varphi_\mathbf{s} d\mathbf{x}.$$

Following [26], the porous volumes are obtained by distributing the porous volume of each cell k to its nodes $\mathbf{s} \in \mathcal{V}_k$. For each $k \in \mathcal{M}$, we define a set of non-negative volume fractions $(a_{k,\mathbf{s}})_{\mathbf{s}\in\mathcal{V}_k\setminus\mathcal{V}_{\rm Dir}}$ satisfying $\sum_{\mathbf{s}\in\mathcal{V}_k\setminus\mathcal{V}_{\rm Dir}} a_{k,\mathbf{s}} < 1$, and we set

$$\phi_{k,\mathbf{s}} = a_{k,\mathbf{s}} \int_k \phi(\mathbf{x}) d\mathbf{x}.$$

Then, we consider for all $k \in \mathcal{M}$ and $\mathbf{s} \in \mathcal{V} \setminus \mathcal{V}_{\rm Dir}$:

$$\phi_k = \int_k \phi(\mathbf{x}) d\mathbf{x} - \sum_{\mathbf{s}\in\mathcal{V}_k\setminus\mathcal{V}_{\rm Dir}} \phi_{k,\mathbf{s}}, \qquad \phi_\mathbf{s} = \sum_{k\in\mathcal{M}_\mathbf{s}} \phi_{k,\mathbf{s}}.$$

It is shown in [26] that the weights $(a_{k,\mathbf{s}})_{\mathbf{s}\in\mathcal{V}_K\setminus\mathcal{V}_{\rm Dir}}$ can be chosen to avoid artificial drain enlargement at nodes sharing cells with highly contrasted permeabilities. Roughly speaking it suffices to select these weights proportional to the permeabilities of the cells $k \in \mathcal{M}_\mathbf{s}$ around a given node $\mathbf{s}$.

3.2 Choice of the primary unknowns

From the conformity assumption of the mesh w.r.t. the rock type partition of the domain, a single rock type $\mathrm{rt}_k \in \mathcal{RT}$ is defined for each cell $k \in \mathcal{M}$. Let us denote by $\chi_\mathbf{s} = \{\mathrm{rt}_k,\, k \in \mathcal{M}_\mathbf{s}\} \subset \mathcal{RT}$ the subset of rock types at the node $\mathbf{s} \in \mathcal{V}$. Let us also set $\chi_k = \{\mathrm{rt}_k\}$ for all $k \in \mathcal{M}$. The choice of the primary unknowns plays an important role to improve the nonlinear convergence of the Newton-Raphson algorithm used to solve the nonlinear system at each time step of the simulation. As usual the first primary unknown is a given phase pressure. To fix ideas, we hereafter consider the non-wetting phase pressure. The second primary unknown

must account for the transmission conditions at the nodes $\mathbf{s}$ located at the interface between different rock types i.e. such that $\#\chi_{\mathbf{s}} \geq 2$. In the following we use the general framework introduced in [13] and based on a parametrization of the monotone graph extensions $\widetilde{P}_{c,\mathrm{rt}}$ of the capillary pressure functions. For each $\nu \in \mathcal{M} \cup \mathcal{V}$, non-decreasing continuous functions

$$\begin{cases} P_{c,\chi_\nu}(\tau), \\ S^{\mathrm{nw}}_{\chi_\nu,\mathrm{rt}}(\tau), \text{for all rt} \in \chi_\nu, \end{cases} \tag{3.2}$$

are built for $\tau \in [0,1]$ such that

$$\begin{cases} P_{c,\chi_\nu}(\tau) \in \widetilde{P}_{c,\mathrm{rt}}(S^{\mathrm{nw}}_{\chi_\nu,\mathrm{rt}}(\tau)), \text{for all rt} \in \chi_\nu, \\ S^{\mathrm{nw}}_{\chi_\nu,\mathrm{rt}}(0) = 0,\ S^{\mathrm{nw}}_{\chi_\nu,\mathrm{rt}}(1) = 1, \text{for all rt} \in \chi_\nu, \\ P_{c,\chi_\nu}(0) = \min_{\mathrm{rt}\in\chi_\nu} P_{c,\mathrm{rt}}(0),\ P_{c,\chi_\nu}(1) = \max_{\mathrm{rt}\in\chi_\nu} P_{c,\mathrm{rt}}(1), \\ P_{c,\chi_\nu}(\tau) + \sum_{\mathrm{rt}\in\chi_\nu} S^{\mathrm{nw}}_{\chi_\nu,\mathrm{rt}}(\tau) \text{ is strictly increasing.} \end{cases}$$

Then, we set

$$S^{\mathrm{w}}_{\chi_\nu,\mathrm{rt}}(\tau) = 1 - S^{\mathrm{nw}}_{\chi_\nu,\mathrm{rt}}(\tau).$$

For the analysis, the functions (3.2) are extended outside the interval $[0,1]$ as follows:

$$\begin{cases} S^{\mathrm{nw}}_{\chi_\nu,\mathrm{rt}}(\tau) = \tau & \text{if } \tau \in \mathbb{R} \setminus [0,1], \\ P_{c,\chi_\nu}(\tau) = P_{c,\chi_\nu}(0) + \tau & \text{if } \tau < 0, \\ P_{c,\chi_\nu}(\tau) = P_{c,\chi_\nu}(1) + \tau - 1 & \text{if } \tau > 1. \end{cases} \tag{3.3}$$

The main advantage of this framework is to incorporate in the construction of the functions (3.2) the saturation jump conditions at different rock type interfaces and to take into account general capillary pressure functions. A first simple example of such construction is simply to set $\tau = s^{\mathrm{nw}}$ for $\#\chi_\nu = 1$ and

$$\tau = \frac{p_c - \min_{\mathrm{rt}\in\chi_\nu} p_{c,\mathrm{rt}}(0)}{\max_{\mathrm{rt}\in\chi_\nu} p_{c,\mathrm{rt}}(1) - \min_{\mathrm{rt}\in\chi_\nu} p_{c,\mathrm{rt}}(0)},$$

for $\#\chi_\nu > 1$. This choice has two drawbacks, it is not robust in terms of nonlinear convergence in dried zones, and it does not apply to non invertible capillary pressure functions such as constant capillary pressures. The second example implemented in the numerical section uses $\tau = s^{\mathrm{nw}}$ for $\#\chi_\nu = 1$ and the parametrization defined in [13] for $\#\chi_\nu > 1$. This parametrization is based on switch of variables and applies to general capillary functions including vanishing capillary diffusion and capillary barriers. We refer to the numerical section for examples of such parametrizations.

Using the above framework, given the primary unknowns $p^{\mathrm{nw}}_{\mathcal{D}} = (p^{\mathrm{nw}}_\nu)_{\nu\in\mathcal{M}\cup\mathcal{V}}$ and $\tau_{\mathcal{D}} = (\tau_\nu)_{\nu\in\mathcal{M}\cup\mathcal{V}}$, we define

$$\begin{cases} p_{c,\mathcal{D}} &= (p_{c,\nu})_{\nu\in\mathcal{M}\cup\mathcal{V}}, & \text{with } p_{c,\nu} = P_{c,\chi_\nu}(\tau_\nu), \\ p^{\mathrm{w}}_{\mathcal{D}} &= (p^{\mathrm{w}}_\nu)_{\nu\in\mathcal{M}\cup\mathcal{V}}, & \text{with } p^{\mathrm{w}}_\nu = p^{\mathrm{nw}}_\nu - p_{c,\nu}, \\ \Phi^\alpha_{\mathcal{D}} &= p^\alpha_{\mathcal{D}} + \rho_\alpha g Z_{\mathcal{D}}, & \text{with } Z_{\mathcal{D}} = (z_\nu)_{\nu\in\mathcal{M}\cup\mathcal{V}}, \\ s^\alpha_k &= S^\alpha_{\chi_k,\mathrm{rt}_k}(\tau_k), & k \in \mathcal{M}, \\ s^\alpha_{k,\mathbf{s}} &= S^\alpha_{\chi_{\mathbf{s}},\mathrm{rt}_k}(\tau_{\mathbf{s}}), & \mathbf{s} \in \mathcal{V},\ k \in \mathcal{M}_{\mathbf{s}}. \end{cases} \tag{3.4}$$

It results from these definitions that the pressures at a given node $\mathbf{s}$ are uniquely defined while the saturations at the node $\mathbf{s}$ depend on the rock type of each cell $k \in \mathcal{M}_{\mathbf{s}}$, capturing the saturation jumps at rock type interfaces, as illustrated in Figure 3. This set of notations is used in the remaining of the paper.

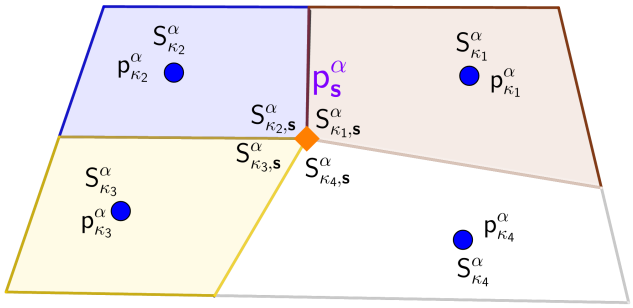

Figure 3: Discrete phase pressures and saturations in the four cells $k_i, i = 1, \cdots, 4$ sharing the vertex $\mathbf{s}$.

3.3 Two-phase Darcy flow VAG discretization

Given the primary unknowns $p_{\mathcal{D}}^{\mathrm{nw}}$ and $\tau_{\mathcal{D}}$, we respectively denote the gravity and capillary gradient VAG fluxes by $G_{k,\mathbf{s}}$ and $C_{k,\mathbf{s}}$ for all $k \in \mathcal{M}$, $\mathbf{s} \in \mathcal{V}_k$. They are defined by

$$\left\{ \begin{array}{l} G_{k,\mathbf{s}} = (\rho_{\mathrm{nw}} - \rho_{\mathrm{w}}) g F_{k,\mathbf{s}}\Big(Z_{\mathcal{D}}\Big), \\ C_{k,\mathbf{s}} = C_{k,\mathbf{s}}(\tau_{\mathcal{D}}) = F_{k,\mathbf{s}}(p_{c,\mathcal{D}}). \end{array} \right. \tag{3.5}$$

The total velocity VAG fluxes are denoted by

$$V_{k,\mathbf{s}}^T = V_{k,\mathbf{s}}^T(p_{\mathcal{D}}^{\mathrm{nw}}, \tau_{\mathcal{D}}),$$

for all $k \in \mathcal{M}$, $\mathbf{s} \in \mathcal{V}_k$. Their definition depend on the approximation of the mobilities and will be discussed in subsection 3.5. Given $V_{k,\mathbf{s}}^T$, $G_{k,\mathbf{s}}$, $C_{k,\mathbf{s}}$, we introduce the following VAG non-wetting phase Darcy fluxes for all $k \in \mathcal{M}$, $\mathbf{s} \in \mathcal{V}_k$:

$$\mathcal{F}_{k,\mathbf{s}}^{\mathrm{nw}}\Big(\tau_k, \tau_{\mathbf{s}}, V_{k,\mathbf{s}}^T, G_{k,\mathbf{s}}, C_{k,\mathbf{s}}\Big),$$

and we define the VAG wetting phase Darcy fluxes by

$$\mathcal{F}_{k,\mathbf{s}}^{\mathrm{w}}\Big(\tau_k, \tau_{\mathbf{s}}, V_{k,\mathbf{s}}^T, G_{k,\mathbf{s}}, C_{k,\mathbf{s}}\Big) = V_{k,\mathbf{s}}^T - \mathcal{F}_{k,\mathbf{s}}^{\mathrm{nw}}\Big(\tau_k, \tau_{\mathbf{s}}, V_{k,\mathbf{s}}^T, G_{k,\mathbf{s}}, C_{k,\mathbf{s}}\Big).$$

The VAG non-wetting phase Darcy fluxes $\mathcal{F}_{k,\mathbf{s}}^{\mathrm{nw}}$ are assumed to satisfy the following continuity, monotonicity and consistency properties.

- **Continuity** : $\mathcal{F}_{k,\mathbf{s}}^{\mathrm{nw}}$ is continuous w.r.t. all its arguments.
- **Monotonicity**: $\mathcal{F}_{k,\mathbf{s}}^{\mathrm{nw}}$ is non-decreasing w.r.t. its first argument and non-increasing w.r.t. its second argument,
- **Consistency**:

  (i) For any $s^{\mathrm{nw}} \in [0,1]$, let $(\tau_k, \tau_{\mathbf{s}})$ be such that $s^{\mathrm{nw}} = s_k^{\mathrm{nw}} = s_{k,\mathbf{s}}^{\mathrm{nw}}$, and set $s^{\mathrm{w}} = 1 - s^{\mathrm{nw}}$. Then, for any $V_{k,\mathbf{s}}^T, G_{k,\mathbf{s}}, C_{k,\mathbf{s}}$, it holds that

$$\mathcal{F}_{k,\mathbf{s}}^{\mathrm{nw}}\Big(\tau_k, \tau_{\mathbf{s}}, V_{k,\mathbf{s}}^T, G_{k,\mathbf{s}}, C_{k,\mathbf{s}}\Big) = f_{\mathrm{rt}_k}^{\mathrm{nw}}(s^{\mathrm{nw}}) V_{k,\mathbf{s}}^T + \frac{\eta_{\mathrm{rt}_k}^{\mathrm{nw}}(s^{\mathrm{nw}}) \eta_{\mathrm{rt}_k}^{\mathrm{w}}(s^{\mathrm{w}})}{\eta_{\mathrm{rt}_k}(s^{\mathrm{nw}})}\Big(G_{k,\mathbf{s}} + C_{k,\mathbf{s}}\Big).$$

  (ii) For all $(\tau_k, \tau_{\mathbf{s}})$ such that $\tau_k \leq 0$ and $\tau_{\mathbf{s}} \leq 0$, and all $V_{k,\mathbf{s}}^T, G_{k,\mathbf{s}}, C_{k,\mathbf{s}}$, it holds that

$$\mathcal{F}_{k,\mathbf{s}}^{\mathrm{nw}}\Big(\tau_k, \tau_{\mathbf{s}}, V_{k,\mathbf{s}}^T, G_{k,\mathbf{s}}, C_{k,\mathbf{s}}\Big) = 0.$$

(iii) For all $(\tau_k, \tau_{\mathbf{s}})$ such that $\tau_k \geq 1$ and $\tau_{\mathbf{s}} \geq 1$, and all $V_{k,\mathbf{s}}^T, G_{k,\mathbf{s}}, C_{k,\mathbf{s}}$, it holds that

$$\mathcal{F}_{k,\mathbf{s}}^{\mathrm{nw}}\Big(\tau_k, \tau_{\mathbf{s}}, V_{k,\mathbf{s}}^T, G_{k,\mathbf{s}}, C_{k,\mathbf{s}}\Big) = V_{k,\mathbf{s}}^T.$$

Remark 3.1. *Let us remark that the consistency properties (i)-(ii)-(iii) result from the extension of the mobilities given by Assumption ($\boldsymbol{A}_4$) combined with the property that for any $(\tau_k, \tau_{\mathbf{s}}) \in \mathbb{R} \times \mathbb{R}$ such that $\eta_{\mathrm{rt}_k}^{\mathrm{nw}}(s_k^{\mathrm{nw}}) = \eta_{\mathrm{rt}_k}^{\mathrm{nw}}(s_{k,\mathbf{s}}^{\mathrm{nw}})$, $\eta_{\mathrm{rt}_k}^{\mathrm{w}}(1 - s_k^{\mathrm{nw}}) = \eta_{\mathrm{rt}_k}^{\mathrm{w}}(1 - s_{k,\mathbf{s}}^{\mathrm{nw}})$, it holds for any $V_{k,\mathbf{s}}^T, G_{k,\mathbf{s}}, C_{k,\mathbf{s}}$ that*

$$\mathcal{F}_{k,\mathbf{s}}^{\mathrm{nw}}\Big(\tau_k, \tau_{\mathbf{s}}, V_{k,\mathbf{s}}^T, G_{k,\mathbf{s}}, C_{k,\mathbf{s}}\Big) = \frac{\eta_{\mathrm{rt}_k}^{\mathrm{nw}}(s_k^{\mathrm{nw}})}{\eta_{\mathrm{rt}_k}(s_k^{\mathrm{nw}})} V_{k,\mathbf{s}}^T + \frac{\eta_{\mathrm{rt}_k}^{\mathrm{nw}}(s_k^{\mathrm{nw}})\eta_{\mathrm{rt}_k}^{\mathrm{w}}(1 - s_k^{\mathrm{nw}})}{\eta_{\mathrm{rt}_k}(s_k^{\mathrm{nw}})}\Big(G_{k,\mathbf{s}} + C_{k,\mathbf{s}}\Big).$$

This last property will hold true for both constructions presented in Subsection 3.5.

The discretization of the accumulation term at each cell and node makes use of the porous volumes $\phi_{k,\mathbf{s}}$, $k \in \mathcal{M}$, $\mathbf{s} \in \mathcal{V}_k \setminus \mathcal{V}_{\mathrm{Dir}}$. More precisely, it is defined by the functions

$$\left\{\begin{array}{ll} \gamma_k^\alpha(\tau) &= S_{\chi_k,\mathrm{rt}_k}^\alpha(\tau), \qquad\qquad k \in \mathcal{M}, \\ \\ \gamma_{\mathbf{s}}^\alpha(\tau) &= \displaystyle\sum_{k \in \mathcal{M}_{\mathbf{s}}} \frac{\phi_{k,\mathbf{s}}}{\phi_{\mathbf{s}}} S_{\chi_{\mathbf{s}},\mathrm{rt}_k}^\alpha(\tau), \quad \mathbf{s} \in \mathcal{V} \setminus \mathcal{V}_{\mathrm{Dir}}. \end{array}\right. \tag{3.6}$$

For $N \in \mathbb{N}^*$, let us consider the time discretization $t^0 = 0 < t^1 < \cdots < t^{n-1} < t^n \cdots < t^N = t_f$ of the time interval $[0, t_f]$. We denote the time steps by $\Delta t^n = t^n - t^{n-1}$ for all $n = 1, \cdots, N$.

Then, for a given $\tau_{\mathcal{D}}^0 \in [0,1]^{\mathcal{M} \cup (\mathcal{V} \setminus \mathcal{V}_{\mathrm{Dir}})}$ at initial time, and given $\tau_{\mathbf{s},Dir} \in [0,1]$, $p_{\mathbf{s},Dir}^{\mathrm{nw}}$, $\mathbf{s} \in \mathcal{V}_{\mathrm{Dir}}$ at the Dirichlet boundary nodes, the scheme looks for $(p_{\mathcal{D}}^{\mathrm{nw},n}, \tau_{\mathcal{D}}^n)$, $n = 1, \cdots, N$ solutions of the following system of equations for $\alpha \in \{\mathrm{nw}, \mathrm{w}\}$:

$$\left\{\begin{array}{l} \dfrac{\phi_k}{\Delta t^n}\Big(\gamma_k^\alpha(\tau_k^n) - \gamma_k^\alpha(\tau_k^{n-1})\Big) \\ \quad + \displaystyle\sum_{\mathbf{s} \in \mathcal{V}_k} \mathcal{F}_{k,\mathbf{s}}^\alpha\Big(\tau_k^n, \tau_{\mathbf{s}}^n, V_{k,\mathbf{s}}^T(p_{\mathcal{D}}^{\mathrm{nw},n}, \tau_{\mathcal{D}}^n), G_{k,\mathbf{s}}, C_{k,\mathbf{s}}(\tau_{\mathcal{D}}^n)\Big) = 0, \quad k \in \mathcal{M}, \\ \\ \dfrac{\phi_{\mathbf{s}}}{\Delta t^n}\Big(\gamma_{\mathbf{s}}^\alpha(\tau_{\mathbf{s}}^n) - \gamma_{\mathbf{s}}^\alpha(\tau_{\mathbf{s}}^{n-1})\Big) \\ \quad - \displaystyle\sum_{k \in \mathcal{M}_{\mathbf{s}}} \mathcal{F}_{k,\mathbf{s}}^\alpha\Big(\tau_k^n, \tau_{\mathbf{s}}^n, V_{k,\mathbf{s}}^T(p_{\mathcal{D}}^{\mathrm{nw},n}, \tau_{\mathcal{D}}^n), G_{k,\mathbf{s}}, C_{k,\mathbf{s}}(\tau_{\mathcal{D}}^n)\Big) = 0, \quad \mathbf{s} \in \mathcal{V} \setminus \mathcal{V}_{\mathrm{Dir}}, \\ \\ p_{\mathbf{s}}^{\mathrm{nw},n} = p_{\mathbf{s},\mathrm{Dir}}^{\mathrm{nw}}, \quad \tau_{\mathbf{s}}^n = \tau_{\mathbf{s},\mathrm{Dir}}, \qquad\qquad \mathbf{s} \in \mathcal{V}_{\mathrm{Dir}}, \end{array}\right. \tag{3.7}$$

Let us point out that, summing the conservation equations over both phases entails that the fluxes $V_{k,\mathbf{s}}^{T,n} = V_{k,\mathbf{s}}^T(p_{\mathcal{D}}^{\mathrm{nw},n}, \tau_{\mathcal{D}}^n)$ fulfill the discrete divergence-free property

$$\sum_{\mathbf{s} \in \mathcal{V}_k} V_{k,\mathbf{s}}^{T,n} = 0 \text{ for all } k \in \mathcal{M}, \quad \sum_{k \in \mathcal{M}_{\mathbf{s}}} V_{k,\mathbf{s}}^{T,n} = 0 \text{ for all } \mathbf{s} \in \mathcal{V} \setminus \mathcal{V}_{\mathrm{Dir}}. \tag{3.8}$$

3.4 Physical bounds on the saturations and existence result

We now focus on two prominent properties of the VAG scheme (3.7) where numerical fluxes $\mathcal{F}_{k,\mathbf{s}}^{nw}$, $k \in \mathcal{M}$, $\mathbf{s} \in \mathcal{V}_k$ are assumed to satisfy the continuity, monotonicity and consistency assumptions. First we prove that any solution of (3.7) satisfies the physical bounds on the saturations. In view of (3.3), this is equivalent to show that $\tau_{\mathcal{D}}^n \in [0,1]^{\mathcal{M}\cup\mathcal{V}}$. Secondly, we establish the existence of a solution of such a finite volume scheme.

Proposition 3.1. *Let be given numerical fluxes $\mathcal{F}_{k,\mathbf{s}}^{nw}$, $k \in \mathcal{M}$, $\mathbf{s} \in \mathcal{V}_k$ satisfying the continuity, monotonicity and consistency assumptions. Then, for a given $\tau_{\mathcal{D}}^0 \in [0,1]^{\mathcal{M}\cup(\mathcal{V}\setminus\mathcal{V}_{\rm Dir})}$ at initial time, and given $\tau_{\mathbf{s},Dir} \in [0,1]$ at Dirichlet boundary nodes $\mathbf{s} \in \mathcal{V}_{\rm Dir}$, any solution $(p_{\mathcal{D}}^{{\rm nw},n}, \tau_{\mathcal{D}}^n)$, $n = 1, \cdots, N$, of the scheme (3.7) satisfies*

$$\tau_{\mathcal{D}}^n \in [0,1]^{\mathcal{M}\cup\mathcal{V}} \text{ for all } n = 1, \cdots, N. \tag{3.9}$$

Proof. Let us set $V_{k,\mathbf{s}}^{T,n} = V_{k,\mathbf{s}}^T(p_{\mathcal{D}}^{{\rm nw},n}, \tau_{\mathcal{D}}^n)$ and $C_{k,\mathbf{s}}^n = C_{k,\mathbf{s}}(\tau_{\mathcal{D}}^n)$ for the sake of shortness. From the Dirichlet boundary condition, the property only needs to be established for all cells and all non Dirichlet nodes. The property $\tau_\nu^n \in [0,1]$ is satisfied by assumption for $n = 0$ for all $\nu \in \mathcal{M} \cup (\mathcal{V} \setminus \mathcal{V}_{\rm Dir})$. Proceeding by induction, for $n \geq 1$, let us assume that $\tau_\nu^{n-1} \in [0,1]$ for all $\nu \in \mathcal{M} \cup (\mathcal{V} \setminus \mathcal{V}_{\rm Dir})$. If there exists $k \in \mathcal{M}$ (to fix ideas) such that

$$\tau_k^n = \min_{\nu\in\mathcal{M}\cup(\mathcal{V}\setminus\mathcal{V}_{\rm Dir})} \tau_\nu^n < 0,$$

then one has

$$\gamma_k^{\rm nw}(\tau_k^{n-1}) = \gamma_k^{\rm nw}(\tau_k^n) + \frac{\Delta t^n}{\phi_k} \sum_{\mathbf{s}\in\mathcal{V}_k} \mathcal{F}_{k,\mathbf{s}}^{\rm nw}\Big(\tau_k^n, \tau_{\mathbf{s}}^n, V_{k,\mathbf{s}}^{T,n}, G_{k,\mathbf{s}}, C_{k,\mathbf{s}}^n\Big).$$

Using the fact that $\gamma_k^{\rm nw}$ is an increasing function on $(-\infty, 0]$ as given in (3.3) we infer that $\gamma_k^{\rm nw}(\tau_k^n) < 0$. According to the monotonicity property of the numerical flux functions $\mathcal{F}_{k,\mathbf{s}}^{\rm nw}$ at fixed $V_{k,\mathbf{s}}^{T,n}, G_{k,\mathbf{s}}, C_{k,\mathbf{s}}^n$, and to their consistency property (ii), it results that

$$\gamma_k^{\rm nw}(\tau_k^{n-1}) < \frac{\Delta t^n}{\phi_k} \sum_{\mathbf{s}\in\mathcal{V}_k} \mathcal{F}_{k,\mathbf{s}}^{\rm nw}\Big(\tau_k^n, \tau_k^n, V_{k,\mathbf{s}}^{T,n}, G_{k,\mathbf{s}}, C_{k,\mathbf{s}}^n\Big) = 0,$$

which leads to a contradiction. The same conclusion remains true if the minimum of $\tau_{\mathcal{D}}^n$ is reached for a node value.

Similarly if there exists $k \in \mathcal{M}$ (to fix ideas) such that

$$\tau_k^n = \max_{\nu\in\mathcal{M}\cup(\mathcal{V}\setminus\mathcal{V}_{\rm Dir})} \tau_\nu^n > 1,$$

then $\gamma_k^{\rm nw}(\tau_k^n) > 1$ since $\gamma_k^{\rm nw}$ is increasing for all $\tau > 1$. Thus, according to the monotonicity property of the numerical flux functions $\mathcal{F}_{k,\mathbf{s}}^{\rm nw}$ at fixed $V_{k,\mathbf{s}}^{T,n}, G_{k,\mathbf{s}}, C_{k,\mathbf{s}}^n$, and to their consistency property (iii), one has

$$\gamma_k^{\rm nw}(\tau_k^{n-1}) > 1 + \frac{\Delta t^n}{\phi_k} \sum_{\mathbf{s}\in\mathcal{V}_k} \mathcal{F}_{k,\mathbf{s}}^{\rm nw}\Big(\tau_k^n, \tau_k^n, V_{k,\mathbf{s}}^{T,n}, G_{k,\mathbf{s}}, C_{k,\mathbf{s}}^n\Big) = 1 + \frac{\Delta t^n}{\phi_k} \sum_{\mathbf{s}\in\mathcal{V}_k} V_{k,\mathbf{s}}^{T,n} = 1,$$

Note that the last equality is obtained thanks to the divergence-free property on the total velocity (3.8). We hence obtain that $\gamma_k^{\rm nw}(\tau_k^{n-1}) > 1$, which yields a contradiction. Again, the same conclusion holds if the maximum of $\tau_{\mathcal{D}}^n$ is reached for a node value. We deduce that the proposition holds for n which concludes the proof by induction. □

Proposition 3.2. *Let be given numerical fluxes $\mathcal{F}^{nw}_{k,\mathbf{s}}$, $k \in \mathcal{M}$, $\mathbf{s} \in \mathcal{V}_k$ satisfying the continuity, monotonicity and consistency assumptions. Let be given $\tau^0_{\mathcal{D}} \in [0,1]^{\mathcal{M}\cup(\mathcal{V}\setminus\mathcal{V}_{\rm Dir})}$ at initial time, and $\tau_{\mathbf{s},Dir} \in [0,1]$ at Dirichlet boundary nodes $\mathbf{s} \in \mathcal{V}_{\rm Dir}$. Let us also assume that the total velocity fluxes $V^{T,n}_{k,\mathbf{s}}$ are given for all $k \in \mathcal{M}$, $\mathbf{s} \in \mathcal{V}_k$ and $n \in \{1,\cdots,N\}$ such that the conservation equations* (3.8) *hold for all $n \in \{1,\cdots,N\}$. Then, there exists a solution $\tau^n_{\mathcal{D}}$, $n = 1,\cdots,N$ of the scheme* (3.7).

Proof. In the sequel, we prove by induction on the time step $n \in \{1,\cdots,N\}$ that there exists $\tau^n_{\mathcal{D}}$ solving the fully implicit finite volume scheme (3.7). The proof is based on Leray-Shauder's topological degree criterion [20]. Let us set $\mathcal{D} = \mathcal{M} \cup \mathcal{V}$ and $\overset{\circ}{\mathcal{D}} = \mathcal{M} \cup (\mathcal{V} \setminus \mathcal{V}_{\rm Dir})$, and let us introduce the mapping $\mathcal{H}$ from $[0,1] \times \mathbb{R}^{\overset{\circ}{\mathcal{D}}}$ to $\mathbb{R}^{\overset{\circ}{\mathcal{D}}}$ defined by

$$\mathcal{H}_k(\mu, \tau_{\overset{\circ}{\mathcal{D}}}) = \frac{\phi_k}{\Delta t^n}\Big(\gamma^{\rm nw}_k(\tau_k) - \gamma^{\rm nw}_k(\tau^{n-1}_k)\Big) + \mu \sum_{\mathbf{s}\in\mathcal{V}_k} \mathcal{F}^{\rm nw}_{k,\mathbf{s}}\Big(\tau_k, \tau_{\mathbf{s}}, V^{T,n}_{k,\mathbf{s}}, G_{k,\mathbf{s}}, C_{k,\mathbf{s}}(\tau_{\mathcal{D}})\Big),$$

$$\mathcal{H}_{\mathbf{s}}(\mu, \tau_{\overset{\circ}{\mathcal{D}}}) = \frac{\phi_{\mathbf{s}}}{\Delta t^n}\Big(\gamma^{\rm nw}_{\mathbf{s}}(\tau_{\mathbf{s}}) - \gamma^{\rm nw}_{\mathbf{s}}(\tau^{n-1}_{\mathbf{s}})\Big) - \mu \sum_{k\in\mathcal{M}_{\mathbf{s}}} \mathcal{F}^{\rm nw}_{k,\mathbf{s}}\Big(\tau_k, \tau_{\mathbf{s}}, V^{T,n}_{k,\mathbf{s}}, G_{k,\mathbf{s}}, C_{k,\mathbf{s}}(\tau_{\mathcal{D}})\Big),$$

for all $k \in \mathcal{M}$ and $\mathbf{s} \in \mathcal{V} \setminus \mathcal{V}_{\rm Dir}$ and where the fixed Dirichlet values $\tau_{\mathbf{s}} = \tau_{\mathbf{s},\rm Dir}, \mathbf{s} \in \mathcal{V}_{\rm Dir}$ are used in the flux functions $\mathcal{F}^{\rm nw}_{k,\mathbf{s}}$. We can then make use of the arguments developed in the proof of Proposition 3.1 to show that any solution of $\mathcal{H}(\mu, \tau_{\overset{\circ}{\mathcal{D}}}) = 0$ satisfies

$$0 \le \tau_\nu \le 1, \text{ for all } \nu \in \mathcal{M} \cup (\mathcal{V} \setminus \mathcal{V}_{\rm Dir}), \text{ for all } \mu \in [0,1].$$

Additionally, the function $\mathcal{H}$ is continuous with respect to $\tau_{\overset{\circ}{\mathcal{D}}}$ and μ thanks to the continuity of the saturations, the flux functions $\mathcal{F}^{\rm nw}_{k,\mathbf{s}}$ and the capillary fluxes $C_{k,\mathbf{s}}$. Now, let us consider B a ball of $\mathbb{R}^{\overset{\circ}{\mathcal{D}}}$ with a sufficiently large radius. For instance, one can take $B = B(0,2)$. As a consequence, there exists no solution fulfilling

$$\mathcal{H}(\mu, \tau_{\mathcal{D}}) = 0,$$

on the boundary of the compact ball $\overline{B} = \overline{B(0,2)}$. Accordingly, the associated topological degree $\text{Degree}(\mathcal{H}(\mu,\cdot), \overline{B})$ is constant for whatever value of μ. In particular, for $\mu = 0$ the scheme is trivially solvable and therefore $\text{Degree}(\mathcal{H}(0,\cdot), \overline{B}) \neq 0$. Thereby, the proposed discrete system obtained for $\mu = 1$ has at least one solution which concludes the proof. □

The proposed discrete framework allows for pure non-wetting and wetting phases on each side of an interface with two different rocktypes. As a result, the uniqueness of the solution for vanishing total velocities might not hold. In any way, it is not known how to address the uniqueness issue in the VAG scheme context due to the non-monotonicity of $C_{k,\mathbf{s}}(\tau^n_{\mathcal{D}})$.

3.5 Examples of numerical fluxes $\mathcal{F}^{\alpha}_{k,\mathbf{s}}$

3.5.1 Phase Potential Upwind (PPU) VAG discretization

The PPU discretization relies on the upwinding of each phase mobility w.r.t. the sign of the phase Darcy flux. In the VAG discretization framework, taking into account the saturation jumps, it leads to the following VAG phase Darcy flux

$$V^{\alpha}_{k,\mathbf{s}} = \eta^{\alpha}_{{\rm rt}_k}(s^{\alpha}_k)\Big(F_{k,\mathbf{s}}(\Phi^{\alpha}_{\mathcal{D}})\Big)^{+} - \eta^{\alpha}_{{\rm rt}_k}(s^{\alpha}_{k,\mathbf{s}})\Big(F_{k,\mathbf{s}}(\Phi^{\alpha}_{\mathcal{D}})\Big)^{-},$$

where we have used the notation $a^{\pm} = \max(\pm a, 0)$ for $a \in \mathbb{R}$. It is a classical approach (see e.g. [6]) already developed for the VAG discretization in [26, 27] and which can be recast in the total velocity formulation framework (3.7) following [10, 22].

3.5.2 Hybrid Upwinding (HU) VAG discretization

The second example is based on the total velocity formulation (2.3) combined with a monotone two-point flux approximation of each fractional flow, gravity and capillary terms separately:

$$\mathcal{F}^{\rm nw}_{k,\mathbf{s}}\Big(\tau_k, \tau_{\mathbf{s}}, V^T_{k,\mathbf{s}}, G_{k,\mathbf{s}}, C_{k,\mathbf{s}}\Big) = \underbrace{f^{\rm nw}_{k,\mathbf{s}}\ V^T_{k,\mathbf{s}}}_{\text{fractional flow flux}} + \underbrace{D^{\rm cap}_{k,\mathbf{s}}\ C_{k,\mathbf{s}}}_{\text{capillary flux}} + \underbrace{D^{\rm g}_{k,\mathbf{s}}\ G_{k,\mathbf{s}}}_{\text{gravity flux}}. \tag{3.10}$$

This type of approach has been introduced in [24, 28] and is known to be more diffusive than the classical PPU approach. Nevertheless, it has been recently shown in [32, 33], in the framework of Two-Point Flux Approximations (TPFA), that these fluxes provide additional robustness of the Newton nonlinear solver, thanks to their additional smoothness property compared with the PPU fluxes. They are termed Hybrid Upwinding (HU) fluxes by the authors [32, 33] and we adopt this terminology in the sequel. We propose here an extension of the HU fluxes to the VAG discretization framework with the following key features:

(i) nodal unknowns at the interface between different rock types allow to capture the saturation jump conditions and contribute to balance the additional diffusion of the HU fluxes versus the PPU fluxes,

(ii) the parametrization framework combined with fully coupled primary unknowns $(p^{\rm nw}, \tau)$ at interfacial nodes allow to account for general capillary pressure functions, including entry pressures and non invertible capillary pressures,

(iii) despite the non monotonicity of the VAG capillary fluxes $C_{k,\mathbf{s}}(\tau^n_{\mathcal{D}}) = F_{K,\mathbf{s}}(p_{c,\mathcal{D}})$, the physical bounds are guaranteed on the variable τ and on the saturations as shown in Proposition 3.1.

We detail below the discretization of each term including the total velocity flux, such that the continuity, monotonicity and consistency properties of the VAG non-wetting phase Darcy fluxes (3.10) are satisfied.

Fractional flow term: an upwind scheme with respect to the discrete total velocity flux $V^T_{k,\mathbf{s}}$ is commonly used as in [28] for the approximation of the fractional flow term. To begin with, we specify the discretization $V^T_{k,\mathbf{s}}$ of the total velocity, setting

$$V^T_{k,\mathbf{s}} = V^T_{k,\mathbf{s}}(p^{\rm nw}_{\mathcal{D}}, \tau_{\mathcal{D}}) = \sum_{\alpha\in\{\rm nw,w\}} \widehat{\eta^{\alpha}_{{\rm rt}_k}}(p^{\rm nw}_{\mathcal{D}}, \tau_{\mathcal{D}}) F_{k,\mathbf{s}}(\Phi^{\alpha}_{\mathcal{D}}), \tag{3.11}$$

where $\widehat{\eta^{\alpha}_{{\rm rt}_k}}(p^{\rm nw}_{\mathcal{D}}, \tau_D)$ is the phase mobility approximation at the interface between the cell k and the node $\mathbf{s}$. Several options are possible for this approximation. First, in the spirit of PPU fluxes, one may consider the standard upwind approximation with respect to the sign of the flux $F_{k,\mathbf{s}}(\Phi^{\alpha}_{\mathcal{D}})$ i.e.

$$\widehat{\eta^{\alpha}_{{\rm rt}_k}}(p^{\rm nw}_{\mathcal{D}}, \tau_{\mathcal{D}}) = \begin{cases} \eta^{\alpha}_{{\rm rt}_k}(s^{\alpha}_k) & \text{if } F_{k,\mathbf{s}}(\Phi^{\alpha}_{\mathcal{D}}) \geq 0, \\ \eta^{\alpha}_{{\rm rt}_k}(s^{\alpha}_{k,\mathbf{s}}) & \text{if } F_{k,\mathbf{s}}(\Phi^{\alpha}_{\mathcal{D}}) < 0. \end{cases} \tag{3.12}$$

Upstream mobilities in the total velocity can not allow a control of the gradient of a reference pressure since the VAG fluxes $F_{k,\mathbf{s}}(\Phi^{\alpha}_{\mathcal{D}})$ are of multi-point nature. This motivates the alternative use of the cell centered approximation defined as follows

$$\widehat{\eta^{\alpha}_{{\rm rt}_k}}(p^{\rm nw}_{\mathcal{D}}, \tau_{\mathcal{D}}) = \eta^{\alpha}_{{\rm rt}_k}(s^{\alpha}_k). \tag{3.13}$$

Note that Propositions 3.1 and 3.2 are established at given total velocities, hence independently of the mobility choice in the total velocity. A numerical comparison between the upwind mobilities (3.12) and the cell centered mobilities (3.13) in the definition of the total velocity flux is presented in Section 4. Finally, the fractional flow approximation uses the classical upwind Godunov monotone scheme

$$f_{k,\mathbf{s}}^{\mathrm{nw}} = f_{k,\mathbf{s}}^{\mathrm{nw}}(\tau_k, \tau_{\mathbf{s}}, V_{k,\mathbf{s}}^T) = \begin{cases} f_{\mathrm{rt_k}}^{\mathrm{nw}}(s_k^{\mathrm{nw}}) & \text{if } V_{k,\mathbf{s}}^T \geq 0, \\ f_{\mathrm{rt_k}}^{\mathrm{nw}}(s_{k,\mathbf{s}}^{\mathrm{nw}}) & \text{if } V_{k,\mathbf{s}}^T < 0. \end{cases} \tag{3.14}$$

Capillary term: in the context of the VAG discretization, as opposed to TPFA discretizations, the capillary gradient flux is not monotone [15, 23]. Hence, undershoots or overshoots on the phase saturations may be generated on poor quality meshes and in the case of strong heterogeneities or anisotropies. To solve this issue, the discretization of the capillary fluxes is performed in the positive methodology thanks to a first order upwind approximation of the mobility terms as performed for instance in [40]. For a parameter $F \in \mathbb{R}$, let us define

$$D_{k,\mathbf{s}}^{\mathrm{up}}(\tau_k, \tau_{\mathbf{s}}, F) = \begin{cases} \dfrac{\eta_{\mathrm{rt}_k}^{\mathrm{nw}}(s_k^{\mathrm{nw}})\eta_{\mathrm{rt}_k}^{\mathrm{w}}(s_{k,\mathbf{s}}^{\mathrm{w}})}{\eta_{\mathrm{rt}_k}(s_k^{\mathrm{nw},n-1})} & \text{if } F \geq 0, \\ \dfrac{\eta_{\mathrm{rt}_k}^{\mathrm{nw}}(s_{k,\mathbf{s}}^{\mathrm{nw}})\eta_{\mathrm{rt}_k}^{\mathrm{w}}(s_k^{\mathrm{w}})}{\eta_{\mathrm{rt}_k}(s_k^{\mathrm{nw},n-1})} & \text{if } F < 0. \end{cases} \tag{3.15}$$

The capillary term is therefore defined by

$$D_{k,\mathbf{s}}^{\mathrm{cap}} = D_{k,\mathbf{s}}^{\mathrm{up}}(\tau_k, \tau_{\mathbf{s}}, C_{k,\mathbf{s}}). \tag{3.16}$$

Gravity term: following [24, 28], the gravity term is discretized using the classical upwind approximation of the mobilities, which can be written as

$$D_{k,\mathbf{s}}^{\mathrm{g}} = D_{k,\mathbf{s}}^{\mathrm{up}}(\tau_k, \tau_{\mathbf{s}}, G_{k,\mathbf{s}}) \tag{3.17}$$

Remark 3.2. *The explicit approximation $\eta_{\mathrm{rt}_k}(s_k^{\mathrm{nw},n-1})$ of the total mobility in* (3.15) *and* (3.17) *is chosen since it leads in practice to a significant improvement in the nonlinear convergence and preserves the monotonicity and consistency properties of the numerical fluxes. The numerical experiments show that this choice does not impair the stability nor the accuracy of the scheme. This can be explained by the much smoother time variation of the total mobilities compared with the variation of the phase mobilities.*

Remark 3.3. *Let us notice an important property of the upwind scheme used in the discretization of capillary diffusion and gravity fluxes. Let us define*

$$D_k(s_k^{\mathrm{nw}}) = \frac{\eta_{\mathrm{rt}_k}^{\mathrm{nw}}(s_k^{\mathrm{nw}})\eta_{\mathrm{rt}_k}^{\mathrm{w}}(s_k^{\mathrm{w}})}{\eta_{\mathrm{rt}_k}(s_k^{\mathrm{nw},n-1})} \geq 0.$$

In view of (3.15) *we observe that*

$$\begin{aligned} \left(D_{k,\mathbf{s}}^{cap}(\tau_k, \tau_{\mathbf{s}}, F) - D_k(s_k^{\mathrm{nw}})\right) F = \; & \frac{\eta_{\mathrm{rt_k}}^{\mathrm{nw}}(s_k^{\mathrm{nw}})}{\eta_{\mathrm{rt}_k}(s_k^{\mathrm{nw},n-1})} \left(\eta_{\mathrm{rt_k}}^{\mathrm{w}}(s_{k,\mathbf{s}}^{\mathrm{w}}) - \eta_{\mathrm{rt_k}}^{\mathrm{w}}(s_k^{\mathrm{w}})\right) F^+ \\ & - \frac{\eta_{\mathrm{rt_k}}^{\mathrm{w}}(s_k^{\mathrm{w}})}{\eta_{\mathrm{rt}_k}(s_k^{\mathrm{nw},n-1})} \left(\eta_{\mathrm{rt_k}}^{\mathrm{nw}}(s_{k,\mathbf{s}}^{\mathrm{nw}}) - \eta_{\mathrm{rt_k}}^{\mathrm{nw}}(s_k^{\mathrm{nw}})\right) F^-. \end{aligned}$$

Therefore since the functions $s \mapsto \eta_{\mathrm{rt_k}}^{\mathrm{nw}}(s)$ and $s \mapsto -\eta_{\mathrm{rt_k}}^{\mathrm{w}}(1-s)$ are non-decreasing, and since the graphs $\widetilde{P}_{c,\mathrm{rt}}$ are monotone, we deduce that

$$D_{k,\mathbf{s}}^{cap}(\tau_k, \tau_{\mathbf{s}}, F)\ F\ (p_{c,k} - p_{c,\mathbf{s}}) \geq D_k(s_k^{\mathrm{nw}})\ F\ (p_{c,k} - p_{c,\mathbf{s}}).$$

An additional asset of the HU VAG finite volume scheme resulting from Remark 3.3 is to ensure a non-negative lower bound on the capillary energy flux term as stated in the following Proposition.

Proposition 3.3. *Let $(p_{\mathcal{D}}^{\mathrm{nw},n}, \tau_{\mathcal{D}}^n)$, $n = 1, \cdots, N$, be a solution of the HU VAG finite volume scheme* (3.7)-(3.10)-(3.11)-(3.14)-(3.15)-(3.17)*. Then, it satisfies*

$$0 \leq \sum_{k\in\mathcal{M}} \sum_{\mathbf{s}\in\mathcal{V}_k} D_{k,\mathbf{s}}^{cap}\Big(\tau_k^n, \tau_{\mathbf{s}}^n, C_{k,\mathbf{s}}(\tau_{\mathcal{D}}^n)\Big) F_{k,\mathbf{s}}(p_{c,\mathcal{D}}^n)(p_{c,k}^n - p_{c,\mathbf{s}}^n). \tag{3.18}$$

Proof. Let us set

$$W_k = \sum_{\mathbf{s}\in\mathcal{V}_k} D_{k,\mathbf{s}}^{\mathrm{cap}}\Big(\tau_k^n, \tau_{\mathbf{s}}^n, C_{k,\mathbf{s}}(\tau_{\mathcal{D}}^n)\Big) F_{k,\mathbf{s}}(p_{c,\mathcal{D}}^n)(p_{c,k}^n - p_{c,\mathbf{s}}^n)$$

In view of Remark 3.3 one has

$$D_{k,\mathbf{s}}^{\mathrm{cap}}\ F_{k,\mathbf{s}}(p_{c,\mathcal{D}})\ (p_{c,k} - p_{c,\mathbf{s}}) \geq D_k(s_k^{\mathrm{nw}})\ F_{k,\mathbf{s}}(p_{c,\mathcal{D}})\ (p_{c,k} - p_{c,\mathbf{s}}).$$

Using (3.1) and $\nabla(\sum_{\mathbf{s}\in\mathcal{V}_k}(p_{c,k}^n - p_{c,\mathbf{s}}^n)\varphi_{\mathbf{s}})|_k = -\nabla\pi_{\mathcal{T}} p_{c,\mathcal{D}}|_k$ implies that

$$W_k \geq D_k(s_k^{\mathrm{nw}}) \int_k \nabla\pi_{\mathcal{T}} p_{c,\mathcal{D}} \cdot \Lambda(\mathbf{x}) \nabla\pi_{\mathcal{T}} p_{c,\mathcal{D}} d\mathbf{x} \geq 0. \tag{3.19}$$

The result follows by summing over the cells k. □

4 Numerical experiments

In this section we perform several numerical experiments whose aim is to compare the robustness and the efficiency of the PPU and HU VAG schemes. We also investigate the impact of the approximation of the total mobility for the HU VAG scheme using either the upwind choice (3.12) denoted by HU-EtaKs, or the centered choice (3.13) denoted by HU-EtaK.

In the following simulations, the time stepping is defined by $\Delta t^1 = \Delta t_{init}$ and for all $n \geq 1$ by

$$\Delta t^{n+1} = \max(\Delta t_{max}, 1.2\Delta t^n),$$

in case of a successful time step Δt^n, and $\Delta t^{n+1} = \dfrac{\Delta t^n}{2}$, in case of non convergence of the Newton algorithm in 25 iterations.

At each time step, the nonlinear system is solved using a Newton algorithm. The cell unknowns are eliminated without any fill-in before solving the linear system using a GMRES iterative algorithm preconditioned by the CPR-AMG preconditioner [43, 36]. To obtain a more robust convergence of the nonlinear solver, a damping of the Newton step forces a maximum variation of 1 of the τ discrete unknown. This strategy is applied for all test cases and all schemes. The GMRES stopping criterion on the relative residual is fixed to 10^{-6}. The Newton solver is convergent if the relative residual is lower than 10^{-5} or if the weighted maximum norm of the Newton increment is lower than 10^{-4}. We denote by $N_{\triangle t}$ the number of successful time steps, by N_{Chop} the number of time step chops, by N_{Newton} the average number of Newton iterations per successful time step, and by N_{GMRES} the average number of GMRES iterations per Newton iteration. Finally, CPU (s) stands for the CPU time in seconds.

4.1 Test problem I : oil migration in a 1D basin with capillary barrier

As exhibited in Figure 4, we consider the basin domain $\Omega = (0, L_x) \times (0, L_y) \times (0, L_z)$ with $L_x = Ly = 10\ m$ and $L_z = 800\ m$ including a drain rock type on $\Omega_2 = (0, L_x) \times (0, L_y) \times (0, \frac{L_z}{2})$ and a barrier rock type on $\Omega_1 = \Omega \setminus \overline{\Omega}_2$. Tables 1 and 2 gather the petrophysical properties of the porous medium as well as the hydrodynamical and thermodynamical laws of the wetting (water) and non-wetting (oil) phases. Note that the permeability and porosity are chosen homogeneous for this test case in order to emphasize the capillary barrier effect at the interface between the drain and barrier subdomains. The basin is initially saturated by water and the oil phase is injected at the bottom boundary $z = 0$ using the Dirichlet input boundary condition $s^{\rm nw} = 0.5$ on the time interval $t \in [0, t_1]$. For $t \in [t_1, t_f]$ the input Dirichlet boundary condition is changed to $s^{\rm nw} = 0$, with $t_1 = 400$ years and $t_f = 800$ years. The pressure is fixed to $p^{\rm nw} = 8.1\ 10^6$ Pa at $z = 0$ and to $p^{\rm w} = 10^5$ Pa at $z = L_z$. The oil phase rises by gravity until it reaches a stationary state corresponding to the trapping of the oil phase in the drain for $z \in (z_{\rm trap}, \frac{L_z}{2})$, with

$$(\rho_{\rm w} - \rho_{\rm nw}) g (\frac{L_z}{2} - z_{\rm trap}) = 6\ 10^5,$$

which yields $z_{\rm trap} = 200$ m with the gravity acceleration set to $g = 10$ m.s^{-2}.

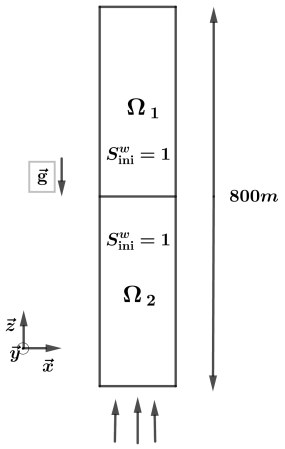

Figure 4: Geometry of the basin with the barrier subdomain Ω_1, the drain subdomain Ω_2, and the initial wetting phase saturation. The non-wetting phase is injected at the bottom boundary during the time interval $[0, t_1]$ using the input boundary condition $s^{\rm nw} = 0.5$.

Quantity	Notation	Dimension	Ω_1	Ω_2
Porosity	ϕ	$[-]$	0.2	0.2
Permeability	Λ	$[m^2]$	10^{-13}	10^{-13}
Relative permeability	$k^\alpha_{r,{\rm rt}}(s^\alpha)$	$[-]$	$(s^\alpha)^2$	$(s^\alpha)^2$
Capillary pressure	$P_{c,{\rm rt}}(s^{\rm nw})$	$[Pa]$	$6.\ 10^5$	0

Table 1: Petrophysical and hydrodynamical properties on the drain Ω_1 and barrier Ω_2 subdomains.

Quantity	Notation	Dimension	Value
Oil density	ρ_{nw}	$[Kg/m^3]$	700
Water density	ρ_{w}	$[Kg/m^3]$	1000
Oil viscosity	μ^{nw}	$[Pa.s]$	0.005
Water viscosity	μ^{w}	$[Pa.s]$	0.001

Table 2: Oil and water phase thermodynamical properties.

The discretization is a uniform Cartesian mesh of size $n_x \times n_y \times n_z$ with $n_x = n_y = 1$ and n_z even. Following [13], the parametrization (3.2) of the capillary pressure graphs is defined by $\tau = s^{\mathrm{nw}}$ for all d.o.f. with a single rock type and is defined by

$$S^{\mathrm{nw}}_{\{\mathrm{rt}_1,\mathrm{rt}_2\},\mathrm{rt}_2}(\tau) = \begin{cases} \tau, & \tau \in [0,1), \\ 1, & \tau \in [1,3], \end{cases} \quad S^{\mathrm{nw}}_{\{\mathrm{rt}_1,\mathrm{rt}_2\},\mathrm{rt}_1}(\tau) = \begin{cases} 0, & \tau \in [0,2), \\ \tau - 2, & \tau \in [2,3], \end{cases}$$

$$P_{c,\{\mathrm{rt}_1,\mathrm{rt}_2\}}(\tau) = \begin{cases} 0, & \tau \in [0,1), \\ 6.\ 10^5(\tau - 1), & \tau \in [1,2), \\ 6.\ 10^5, & \tau \in [2,3], \end{cases}$$

at all nodes located at the interface between both rock types at $z = \frac{L_z}{2}$ (see Figure 5).

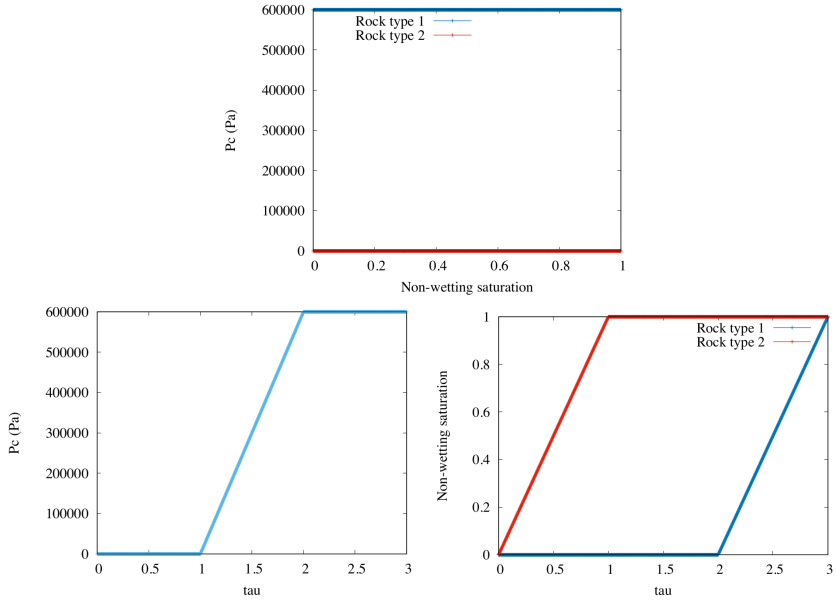

Figure 5: (Top): capillary pressure as a function of the non-wetting phase saturation for both rock types. (Bottom): capillary pressure and non-wetting phase saturations as functions of the parameter $\tau \in [0,3]$.

From Figure 6, one can check that the HU VAG scheme is, as could be expected, slightly more diffusive than the PPU VAG scheme. On the other hand, both schemes capture in an excellent way the saturation jump at the interface between both rock types and they are fully matched on the fine mesh. Figure 7 exhibits that, even on the coarse mesh, there is no significant differences between the centered and the upwind choice of the mobilities in the definition of the total velocity for this test case. The numerical performance of the nonlinear solver is exhibited on Figure 8 using a coarse time stepping defined by $\Delta t_{init} = 1$ year and $\Delta t_{max} = 10$ years

on the fine mesh $n_z = 200$. It is clearly seen that the HU VAG schemes are significantly more efficient than the PPU VAG scheme even on this 1D test case.

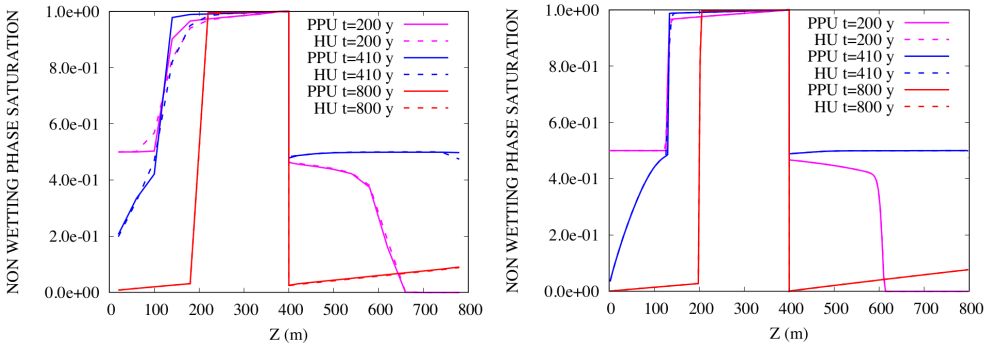

Figure 6: Test I : non-wetting phase saturations as a function of z at different times $t = 200, 410, 800$ years, obtained for the PPU and HU-EtaK VAG schemes both on the 200 cells (right) and 20 cells (left) meshes.

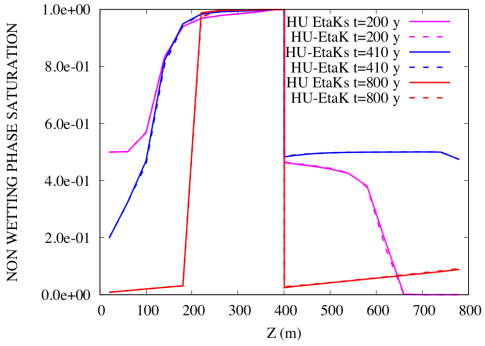

Figure 7: Test I : non-wetting phase saturations as a function of z at different times $t = 200, 410, 800$ years, obtained for the HU-EtaK and HU-EtaKs VAG schemes on the 20 cells mesh.

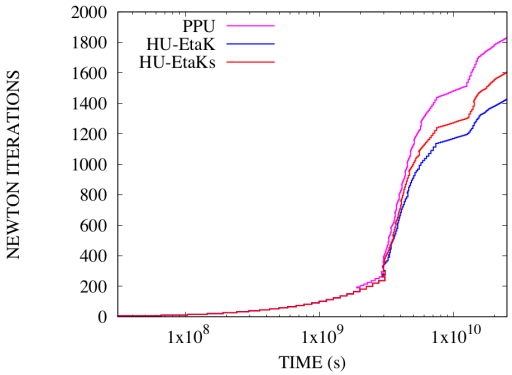

Figure 8: Test I : accumulated number of Newton iterations as a function of time for the PPU, HU-EtaK and HU-EtaKS VAG schemes on the 200-cell mesh with large time steps.

4.2 Test problem II : Large DFM test case

This test case compares the robustness of the PPU and HU VAG schemes on a large 3D Discrete Fracture Matrix (DFM) model using the continuous pressure two-phase Darcy flow model described for example in [12, 13]. The PPU VAG scheme for such two-phase DFM models was discussed in [12, 13] and the HU VAG scheme can be readily extended to such DFM models.

The DFM model is exhibited in Figure 9 with the domain $\Omega = (0, 85) \times (0, 60) \times (0, 140)$ m, it has been kindly provided by the authors of the Benchmark [7, 8]. The matrix rock type is denoted by m and the fracture network rocktype by f. The fracture aperture is set to $d_f = 1$ cm and the fracture network is homogeneous with isotropic tangential permeability $\Lambda_f = 10^{-11}$ m^2 and porosity $\phi_f = 0.2$. The matrix is homogeneous with isotropic permeability $\Lambda_m = 10^{-14}$ m^2 and porosity $\phi_m = 0.4$.

The relative permeabilities are defined by $k^\alpha_{r,f}(s^\alpha) = (s^\alpha)^{1.2}$ and $k^\alpha_{r,m}(s^\alpha) = (s^\alpha)^2$, $\alpha \in \{\mathrm{nw}, \mathrm{w}\}$ and the capillary pressure is fixed to $P_{c,m}(s^{\mathrm{nw}}) = -b_m \log(1 - s^{\mathrm{nw}})$, $b_m = 10^4$ Pa in the matrix and to $P_{c,f}(s^{\mathrm{nw}}) = -b_f \log(1 - s^{\mathrm{nw}})$, $b_f = 10^3$ Pa in the fracture network. The fluid dynamic viscosities and mass densities are already defined in Table 2.

The reservoir is initially saturated with the wetting phase. Dirichlet boundary conditions are imposed at the output boundary $\{0, 85\} \times (0, 20) \times (110, 140)$ with a wetting phase pressure of $p^{\mathrm{w}} = 2.\ 10^6 - \rho_{\mathrm{w}} g z$ Pa and $s^{\mathrm{w}}_m = 1$, as well as at the input boundary $\{0\} \times (40, 60) \times (0, 30) \cup (0, 30) \times (40, 85) \times \{0\}$ with $s^{\mathrm{nw}}_m = 0.9$ and $p^{\mathrm{w}} = 4.\ 10^6 - \rho_{\mathrm{w}} g z$ Pa. The remaining boundaries are impervious and the final simulation time is fixed to $t_f = 3600$ days. The time stepping is defined by $\Delta t_{init} = 0.1$ day, and $\Delta t_{max} =$ 100 days.

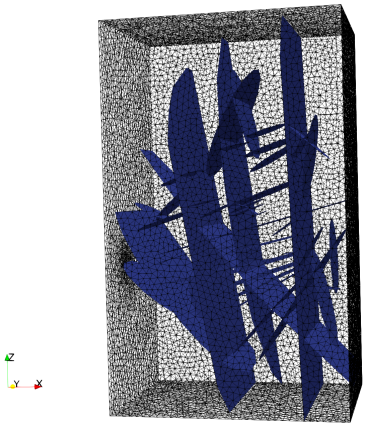

Figure 9: Large DFM model meshed with 495233 tetrahedra and 66908 fracture faces.

Following [13], the parametrization (3.2) of the capillary pressure graphs is defined by $\tau = s^{\mathrm{nw}}$ for all cells and for all nodes not belonging to the fracture network, and is defined by

$$S^{\mathrm{nw}}_{\{m,f\},f}(\tau) = \begin{cases} \tau, & \tau \in [0, \tau_1), \\ 1 - (\tau_1 + (1 - \tau_1)^{\frac{b_f}{b_m}} - \tau)^{\frac{b_m}{b_f}}, & \tau \in [\tau_1, \tau_2), \end{cases} \tag{4.1}$$

$$S^{\mathrm{nw}}_{\{m,f\},m}(\tau) = \begin{cases} 1 - (1 - \tau)^{\frac{b_f}{b_m}}, & \tau \in [0, \tau_1), \\ \tau - \tau_1 + 1 - (1 - \tau_1)^{\frac{b_f}{b_m}}, & \tau \in [\tau_1, \tau_2), \end{cases} \tag{4.2}$$

$$P_{c,\{m,f\}}(\tau) = \begin{cases} -b_f \ln(1-\tau), & \tau \in [0, \tau_1), \\ -b_m \ln(\tau_1 + (1-\tau_1)^{\frac{b_f}{b_m}} - \tau), & \tau \in [\tau_1, \tau_2), \end{cases} \tag{4.3}$$

at all fracture nodes and faces, with $\tau_1 = 1 - (\frac{b_f}{b_m})^{\frac{b_m}{b_m - b_f}}$ and $\tau_2 = \tau_1 + (1-\tau_1)^{\frac{b_f}{b_m}}$ (see Figure 10).

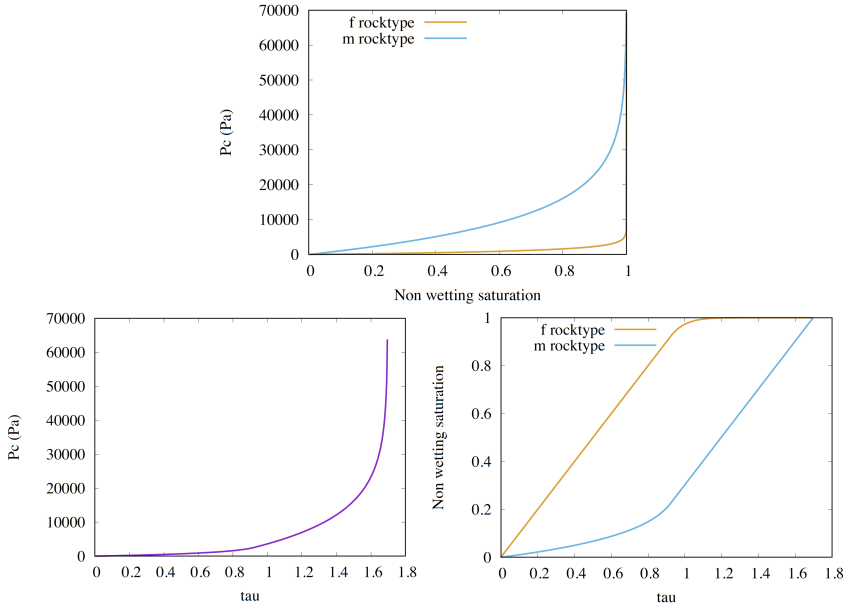

Figure 10: (Top): capillary pressure as a function of the non-wetting phase saturation for both the fracture (f) and matrix (m) rock types with $b_m = 10^4$ and $b_f = 10^3$ Pa. (Bottom): capillary pressure and fracture and matrix non-wetting phase saturations as functions of the parameter $\tau \in [0, \tau_2)$.

Figure 11 exhibits very small differences between the saturations obtained by the PPU and HU-EtaK VAG schemes. The same result has been checked between the HU-EtaK and EtaKs VAG schemes. Table 3 and the left Figure 12 compare the numerical efficiency of the three VAG schemes, showing again a nonlinear convergence of the HU schemes both more robust (no time step failure for HU against 4 time step chops for PPU) and more efficient (average of 4 Newton iterations for HU against almost 7 for PPU) resulting in an overall gain in CPU time of a factor roughly 2 in favor of the HU VAG schemes. The right Figure 12 exhibits the CFL numbers in the matrix and in the fracture network computed for a tracer transported by the total velocity field with the time steps of the VAG HU-EtaKs simulation. One can check that the time steps used in this simulation are at the scale of the matrix transport resulting in very large CFL numbers in the fracture network.

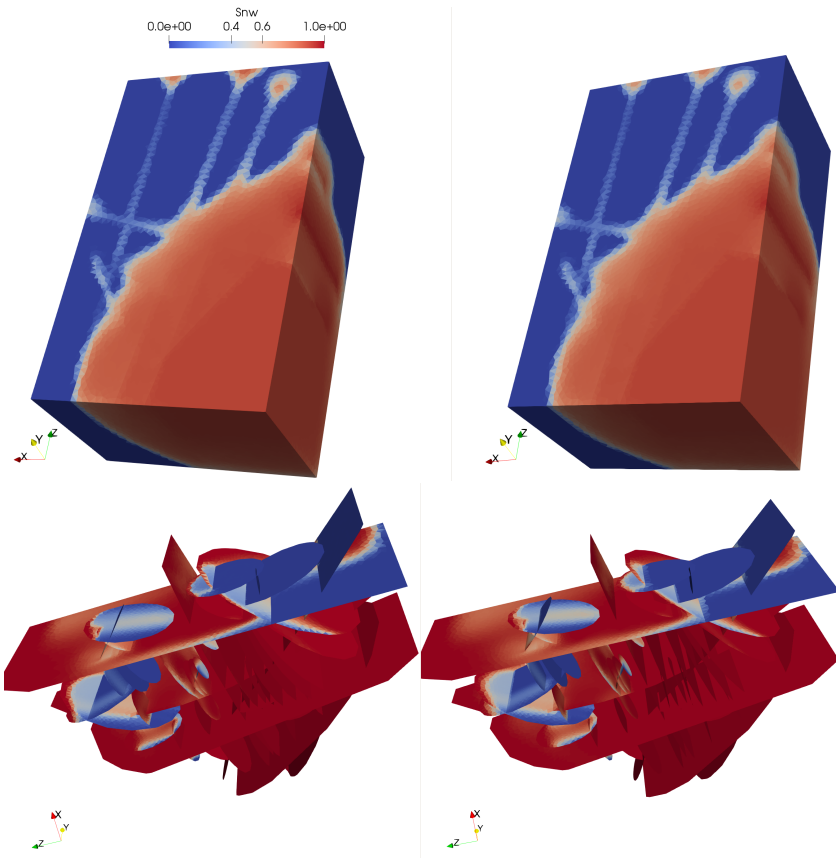

Figure 11: Test II : non-wetting phase saturation in the matrix (top) and in the fracture network (bottom) at final simulation time obtained for the PPU (left) and HU-EtaK (right) VAG schemes.

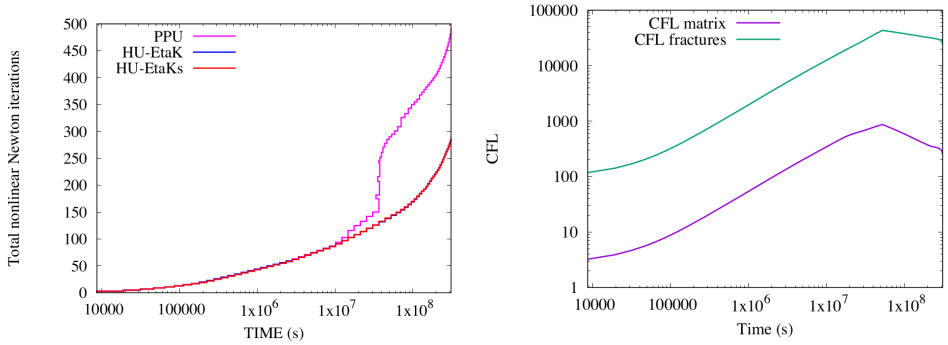

Figure 12: Test II : (left): accumulated number of Newton iterations as a function of time for the different VAG schemes. (Right): CFL numbers in the matrix and in the fracture network as a function of time computed for a tracer transported by the total velocity field with the total velocity field and time steps of the VAG HU-EtaKs simulation.

Scheme	$\#\mathcal{M}$	$N_{\Delta t}$	N_{chop}	N_{Newton}	N_{GMRes}	CPU (s)
VAG PPU	495k cells	80	4	6.8	28	8200
VAG HU-EtaKs	495k cells	69	0	4.1	32	4492
VAG HU-EtaK	495k cells	69	0	4.0	31	4094

Table 3: Test II : numerical behavior of the simulation for the large DFM test case.

4.3 Test problem III : ORUNI DFM test case

This test case considers the large DFM model exhibited in Figure 13 with $\Omega = (0, 300)^3$ m. The Discrete Fracture Network (DFN) including 1000 fractures is derived from the ORUNI network described in [19]. This DFN and its triangulation has been kindly provided by the authors. Then, the 3D mesh has been generated by Patrick Laug starting from the triangulation of the DFN and using the mesh generation tools described in [29]. The quality of the DFN triangulation and of the subsequent tetrahedralization clearly play an essential role in the numerical performance of the simulation.

The fracture aperture is set to $d_f = 1$ cm and the fracture network is homogeneous with isotropic tangential permeability $\Lambda_f = 10^{-10}$ m^2 and porosity $\phi_f = 0.2$. The matrix is homogeneous with porosity $\phi_m = 0.4$ and isotropic permeability Λ_m either equal to 10^{-13} m^2 or 10^{-16} m^2.

The relative permeabilities are defined by $k^{\alpha}_{r,f}(s^{\alpha}) = s^{\alpha}$ and $k^{\alpha}_{r,m}(s^{\alpha}) = (s^{\alpha})^2$, $\alpha \in \{\mathrm{nw}, \mathrm{w}\}$ and the capillary pressure is fixed to $P_{c,m}(s^{\mathrm{nw}}) = -b_m \log(1 - s^{\mathrm{nw}})$, $b_m = 10^5$ Pa in the matrix and to $P_{c,f}(s^{\mathrm{nw}}) = -b_f \log(1 - s^{\mathrm{nw}})$, $b_f = 10^3$ Pa in the fracture network. The fluid dynamic viscosities and mass densities are defined in Table 2.

The reservoir is initially saturated with the wetting phase. Dirichlet boundary conditions are imposed at the top boundary with a wetting phase pressure $p^{\mathrm{w}} = 10^7$ Pa and saturation $s^{\mathrm{w}}_m = 1$. At the bottom boundary a uniform non-wetting phase flow rate is injected in the fractures with a total flow rate of 22.6 m^3 per day. The remaining boundaries are impervious and the final simulation time is fixed to $t_f = 5400$ days. The time stepping is defined by $\Delta t_{init} = 1$ day, and $\Delta t_{max} = 180$ days.

Figure 14 exhibits that the saturation solutions obtained at final simulation time by the PPU and HU-EtaKs schemes for $\Lambda_m = 10^{-13}$ m^2 are very close. Table 4 and the left Figure 15 compare the numerical behavior of both discretizations. The HU version appears again much more robust providing much fewer time step chops than the PPU scheme for $\Lambda_m = 10^{-13}$ m^2. Consequently the time steps are much smaller for the PPU simulation which also results in a lower average number of GMRES iterations and similar average numbers of Newton iterations per successful time step. All together the HU-EtaKs simulation is 2.7 times faster than the PPU simulation. The right Figure 15 exhibits, as in the previous test case, the very large CFL numbers in the fracture network typical of time steps at the scale of the matrix. For the high matrix fracture permeability ratio, with $\Lambda_m = 10^{-16}$ m^2, the PPU simulation has been stopped after more than 100 time step chops for which it has only reached the simulation time of roughly 90 days in 373 time steps and more than 4000 Newton iterations. The Newton solver oscillates even for relatively small time steps preventing the time step from increase sufficiently. On the other hand, the VAG HU scheme is able to simulate this highly heterogeneous large DFM test case in a reasonable amount of time steps.

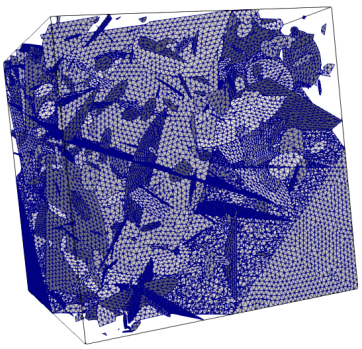

Figure 13: DFM model with the ORUNI DFN of 1000 fractures [19] meshed with 1.7 10^6 tetrahedra [29].

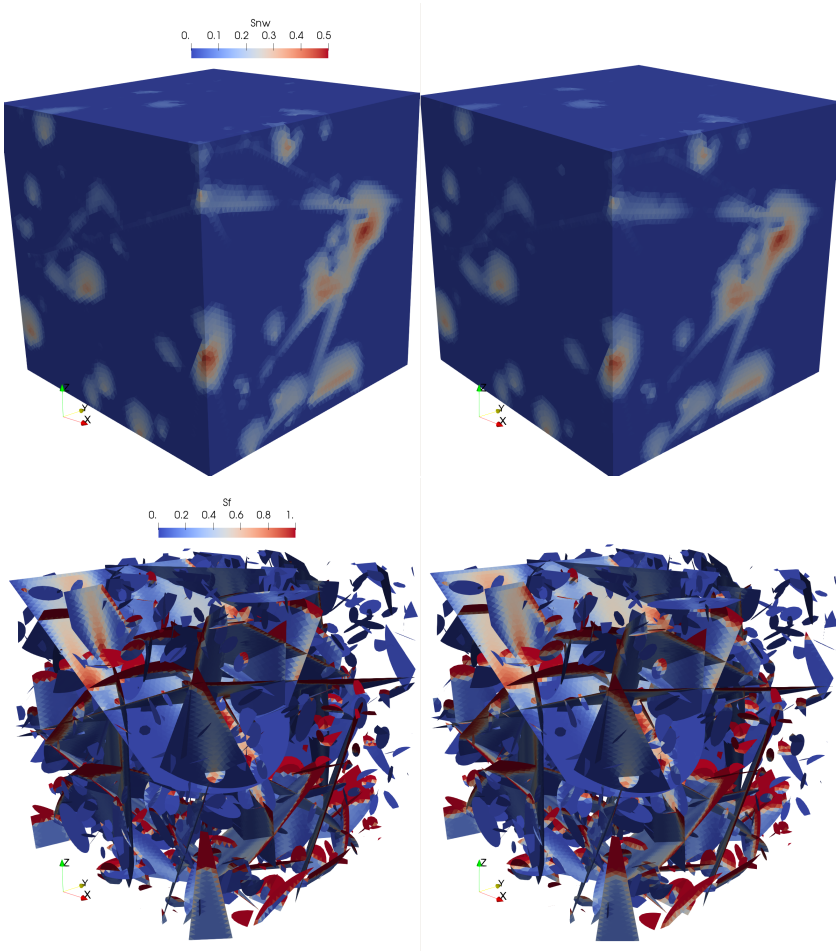

Figure 14: Test III : non-wetting phase saturation in the matrix (top) and in the fracture network (bottom) at final simulation time obtained for $\Lambda_m = 10^{-13}$ m^2 with the PPU (left) and HU-EtaKs (right) VAG schemes.

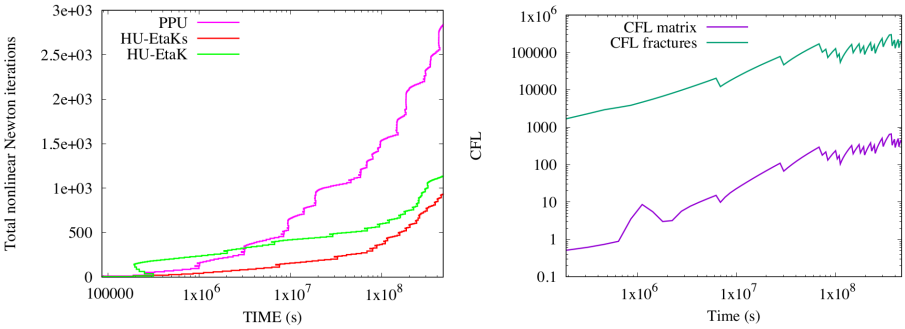

Figure 15: Test III : (left): accumulated number of Newton iterations as a function of time for the VAG PPU, HU-EtaKs and HU-EtaK VAG schemes for $\Lambda_m = 10^{-13}$ m^2. (Right): CFL numbers in the matrix and in the fracture network as a function of time computed for a tracer transported by the total velocity field with the total velocity field and time steps of the VAG HU-EtaKs simulation.

Scheme	$\frac{\Lambda_f}{\Lambda_m}$	$N_{\Delta t}$	N_{chop}	N_{Newton}	N_{GMRes}	CPU (s)
VAG PPU	10^3	245	57	11.6	12	104500
VAG HU-EtaKs	10^3	87	15	10.8	18	38500
VAG HU-EtaK	10^3	115	21	9.9	15	45200
VAG PPU	10^6	x	x	x	x	x
VAG HU-EtaK	10^6	261	62	14.6	26.4	160000

Table 4: Test III : numerical behavior of the simulation for the ORUNI DFM test cases.

5 Conclusions

In this article, the combination of the VAG discretization for the approximation of the gradient fluxes with the HU approximation of the mobility terms in the saturation equation is shown to provide additional robustness compared with the usual PPU approximation of the mobilities on highly heterogeneous two-phase Darcy flow test cases. The nodal interface unknowns allow to capture the saturation jumps at the interfaces between different rock types, providing comparable accuracy for both the HU and PPU VAG schemes on heterogeneous test cases. Thanks to this additional robustness and to the efficiency of nodal discretizations on tetrahedral meshes, the HU VAG scheme makes possible the simulation of large and highly heterogeneous DFM models as exhibited in the numerical section. In perspective, we plan to investigate the efficiency of the HU VAG scheme for the simulation of two-phase Darcy flow discontinuous pressure DFM models accounting for fractures acting both as barrier or drains for which the PPU VAG scheme has been introduced in [14].

Acknowledgments

The authors would like to thank the French National Research Agency for its support in the framework of the CHARMS ANR project ANR-16-CE06-0009.

References

[1] J. Aghili, K. Brenner, J. Hennicker, R. Masson, and L. Trenty. Two-phase Discrete Fracture Matrix models with linear and nonlinear transmission conditions. *GEM-International Journal on Geomathematics*, 10(1):1, 2019.

[2] E. Ahmed, J. Jaffré, and J. E. Roberts. A reduced fracture model for two-phase flow with different rock types. *Mathematics and Computers in Simulation*, 7:49–70, 2017.

[3] R. Ahmed, Y. Xie, and M. G. Edwards. A Cell-Centred CVD-MPFA Finite Volume Method for Two-Phase Fluid Flow Problems with Capillary Heterogeneity and Discontinuity. *Transport in Porous Media*, 127:35–52, 2019.

[4] A. H. Alali, F. P. Hamon, B. P. Mallison, and H. A. Tchelepi. Finite-Volume Simulation of Capillary-Dominated Flow in Matrix-Fracture Systems using Interface Conditions, 2019.

[5] B. Andreianov, K. Brenner, and C. Cancès. Approximating the vanishing capillarity limit of two-phase flow in multi-dimensional heterogeneous porous medium. *ZAMM - Journal of Applied Mathematics and Mechanics / Zeitschrift für Angewandte Mathematik und Mechanik*, 94(7-8):655–667, 2014.

[6] K. Aziz and A. Settari. *Petroleum Reservoir Simulation*. Elsevier, London, 1979.

[7] I. Berre, W. Boon, B. Flemisch, A. Fumagalli, D. Gläser, E. Keilegavlen, A. Scotti, I. Stefansson, and A. Tatomir. Call for participation: Verification benchmarks for single-phase flow in three-dimensional fractured porous media, 2018.

[8] I. Berre, W. M. Boon, B. Flemisch, A. Fumagalli, D. Gläser, E. Keilegavlen, A. Scotti, I. Stefansson, A. Tatomir, K. Brenner, S. Burbulla, P. Devloo, O. Duran, M. Favino, J. Hennicker, I.-H. Lee, K. Lipnikov, R. Masson, K. Mosthaf, M. C. G. Nestola, C.-F. Ni, K. Nikitin, P. Schädle, D. Svyatskiy, R. Yanbarisov, and P. Zulian. Verification benchmarks for single-phase flow in three-dimensional fractured porous media. *arXiv e-prints 2002.07005*, Feb 2020.

[9] I. I. Bogdanov, V. V. Mourzenko, J.-F. Thovert, and P. M. Adler. Two-phase flow through fractured porous media. *Physical Review E*, 68(2), aug 2003.

[10] Y. Brenier and J. Jaffré. Upstream differencing for multiphase flow in reservoir simulation. *SIAM journal on numerical analysis*, 28(3):685–696, 1991.

[11] K. Brenner, C. Cancès, and D. Hilhorst. Finite volume approximation for an immiscible two-phase flow in porous media with discontinuous capillary pressure. *Computational Geosciences*, 17(3):573–597, 2013.

[12] K. Brenner, M. Groza, C. Guichard, and R. Masson. Vertex approximate gradient scheme for hybrid dimensional two-phase Darcy flows in fractured porous media. *ESAIM: Mathematical Modelling and Numerical Analysis*, 49(2):303–330, 2015.

[13] K. Brenner, M. Groza, L. Jeannin, R. Masson, and J. Pellerin. Immiscible two-phase Darcy flow model accounting for vanishing and discontinuous capillary pressures: application to the flow in fractured porous media. *Computational Geosciences*, 21(5-6):1075–1094, 2017.

[14] K. Brenner, J. Hennicker, R. Masson, and P. Samier. Hybrid-dimensional modelling of two-phase flow through fractured porous media with enhanced matrix fracture transmission conditions. *Journal of Computational Physics*, 357:100–124, 2018.

[15] K. Brenner and R. Masson. Convergence of a Vertex Centred Discretization of Two-Phase Darcy flows on General Meshes. *International Journal on Finite Volumes*, 10:1–37, 2013.

[16] C. Cancès. Finite volume scheme for two-phase flows in heterogeneous porous media involving capillary pressure discontinuities. *Mathematical Modelling and Numerical Analysis*, 43:973–1001, 2009.

[17] C. Cancès and M. Pierre. An existence result for multidimensional immiscible two-phase flows with discontinuous capillary pressure field. *SIAM J. Math. Anal.*, 44:966–992, 2012.

[18] G. Chavent and J. Jaffré. *Mathematical models and finite elements for reservoir simulation: single phase, multiphase and multicomponent flows through porous media*, volume 17. Elsevier, North-Holland, Amsterdam, stud. math. appl. edition, 1986.

[19] J.-R. de Dreuzy, G. Pichot, B. Poirriez, and J. Erhel. Synthetic benchmark for modeling flow in 3D fractured media. *Computers and Geosciences*, 50:59 – 71, 2013.

[20] K. Deimling. *Nonlinear Functional Analysis*. Springer-Verlag, Berlin, 1985.

[21] G. Enchéry, R. Eymard, and A. Michel. Numerical approximation of a two-phase flow problem in a porous medium with discontinuous capillary forces. *SIAM Journal on Numerical Analysis*, 43(6):2402–2422, 2006.

[22] G. Enchéry, R. Masson, S. Wolf, and R. Eymard. Mathematical and numerical study of an industrial scheme for two-phase flows in porous media under gravity. *Computational Methods in Applied Mathematics*, 2(4):325–353, 2002.

[23] R. Eymard, T. Gallouët, C. Guichard, R. Herbin, and R. Masson. TP or not TP, that is the question. *Computational Geosciences*, 18(3-4):285–296, 2014.

[24] R. Eymard, T. Gallouët, and P. Joly. Hybrid Finite Element Techniques for Oil Recovery Simulation. *Computer Methods in Applied Mechanics and Engineering*, 74, 1989.

[25] R. Eymard, C. Guichard, and R. Herbin. Small-stencil 3D schemes for diffusive flows in porous media. *ESAIM: Mathematical Modelling and Numerical Analysis*, 46:265–290, 2010.

[26] R. Eymard, C. Guichard, R. Herbin, and R. Masson. Vertex-centred discretization of multiphase compositional Darcy flows on general meshes. *Computational Geosciences*, 16(4):987–1005, 2012.

[27] R. Eymard, C. Guichard, R. Herbin, and R. Masson. Gradient schemes for two-phase flow in heterogeneous porous media and Richards equation. *ZAMM-Journal of Applied Mathematics and Mechanics/Zeitschrift für Angewandte Mathematik und Mechanik*, 94(7-8):560–585, 2014.

[28] T. Gallouët and A. Pfertzel. On some upstream weighting schemes for oil recovery simulation. *Les Annales de l'Enit*, 4(2), 1990.

[29] P. George, H. Borouchaki, F. Alauzet, P. Laug, A. Loseille, and L. Maréchal. *Meshing Geometric Modeling and Numerical Simulation 2 - Metrics Meshes and Mesh Adaptation*. Wiley-ISTE, 2019.

[30] M. Ghilani, E. H. Quenjel, and M. Saad. Positive control volume finite element scheme for a degenerate compressible two-phase flow in anisotropic porous media. *Computational Geosciences*, 23(1):55–79, 2019.

[31] D. Gläser, R. Helmig, B. Flemish, and H. Class. A discrete fracture model for two-phase flow in fractured porous media. *Advances in Water Resources*, 110:335–348, 2017.

[32] F. P. Hamon, B. T. Mallison, and H. A. Tchelepi. Implicit Hybrid Upwind scheme for coupled multiphase flow and transport with buoyancy. *Computer Methods in Applied Mechanics and Engineering*, 311:599–624, 2016.

[33] F. P. Hamon, B. T. Mallison, and H. A. Tchelepi. Implicit hybrid upwinding for two-phase flow in heterogeneous porous media with buoyancy and capillarity. *Computer Methods in Applied Mechanics and Engineering*, 331:701–727, 2018.

[34] J. Hoteit and A. Firoozabadi. An efficient numerical model for incompressible two-phase flow in fracture media. *Advances in Water Resources*, 31:891–905, 2008.

[35] M. Karimi-Fard, L. Durlofsky, and K. Aziz. An efficient discrete-fracture model applicable for general-purpose reservoir simulators. *SPE Journal*, 2004.

[36] S. Lacroix, Y. V. Vassilevski, and M. F. Wheeler. Decoupling preconditioners in the implicit parallel accurate reservoir simulator (IPARS). *Numerical Linear Algebra with Applications*, 8(8):537–549, dec 2001.

[37] K. Mitra and I. S. Pop. A modified L-scheme to solve nonlinear diffusion problems. *Computers & Mathematics with Applications*, 77(6):1722–1738, 2019.

[38] J. Monteagudu and A. Firoozabadi. Control-volume model for simulation of water injection in fractured media: incorporating matrix heterogeneity and reservoir wettability effects. *SPE Journal*, 12:355–366, 2007.

[39] D. W. Peaceman. *Fundamentals of numerical reservoir simulation*, volume 6. Elsevier, 2000.

[40] E. H. Quenjel. Enhanced positive vertex-centered finite volume scheme for anisotropic convection-diffusion equations. *Accpeted in ESAIM Mathematical Modelling and Numerical Analysis /DOI : 10.1051/m2an/2019075*, 2019.

[41] F. A. Radu, J. M. Nordbotten, I. S. Pop, and K. Kumar. A robust linearization scheme for finite volume based discretizations for simulation of two-phase flow in porous media. *Journal of Computational and Applied Mathematics*, 289:134–141, 2015.

[42] V. Reichenberger, H. Jakobs, P. Bastian, and R. Helmig. A mixed-dimensional finite volume method for two-phase flow in fractured porous media. *Advances in Water Resources*, 29(7):1020–1036, jul 2006.

[43] R. Scheichl, R. Masson, and J. Wendebourg. Decoupling and block preconditioning for sedimentary basin simulations. *Computational Geosciences*, 7(4):295–318, 2003.

[44] C. J. Van Duijn, J. Molenaar, and M. J. De Neef. The effect of capillary forces on immiscible two-phase flow in heterogeneous porous media. *Transport in Porous Media*, 21(1):71–93, 1995.

[45] Y. Xie and M. G. Edwards. Unstructured CVD-MPFA Reduced-Dimensional DFM Models for Two-Phase Flow, Coupled with Higher Resolution Hybrid Upwind Methods. *SPE*, 193886-MS, 2019.